THESIS

Micromagnetic modeling of skyrmion dynamics and THz oscillation in antiferromagnets

Cycle

XXXII

Dissertation with the aim of achieving a doctoral degree in
Fundamental Physics
at the Department of Mathematical and Computer Sciences,
Physical Sciences and Earth Sciences,
and at the Department of Science and Technology

of University of Messina and the Lebanese University

Coordinator: Prof. Lorenzo Torrisi

Signature _____

Supervisors: Prof. Giovanni Finocchio
Signature _____

Prof. Fouad El Haj Hassan
Signature _____

Co-Supervisor: Prof. Abbas Hamadeh
Signature _____

Ph. D. student: Dr. Israa Medlej

Signature _____

Abstract

The main goal of this thesis is the achievement of further understanding on various hot topics related to Spintronics.

The name Spintronics is a combination word made of *spin* and *electronics*. Electronics concerns the creation and control of electron currents via their charge, which is well known as *charge current*, while the spin provides a new option to control the charge currents. This connection between electron charge and spin admits to change the electronic transport by spins, and, on the contrary, to alter the magnetic properties by electron charges. Thus, nowadays, the spin is fundamental for some of our technologies due to their interesting properties: nanometer dimension, low energy consumption, non-volatility, high scalability, large speed.

Spintronic devices are usually composed of a trilayer where two ferromagnets are separated by a nonmagnetic spacer. One among of two ferromagnets layer can be manipulated by an external applied field as well as by a polarized electric current injected into the layer. This property gives rise to different technological applications of spintronic devices, importantly, as magnetic storages, which have seen a wide range in commercialization.

In this thesis, two main topics have been investigated. Firstly, we have investigated the magnetic skyrmion dynamics in ferromagnetic materials. Secondly, we have investigated the antiferromagnetic dynamics.

The main contributions of this thesis to the first topic has been about magnetic skyrmions which are chiral spin textures characterized by a non-uniform distribution of the magnetization. They have found widespread range of applications because they can be easily nucleated, moved and shifted by spin polarized current. The center of our attraction is the dynamics of skyrmions driven by the spin-hall effect in a synthetic antiferromagnet. We carried out a theoretical study based on micromagnetic simulations, at room temperature, in presence of thermal fluctuations. We notice that the motion of the skyrmion follows a stochastic flow of motion. Hence, this result paves the way to use skyrmions as building blocks of random bit generators, which can be very useful in modern technology. Another study has been made about the skyrmion topic. We prove that thermal fluctuations excite at least two nonstationary thermal modes which deeply affect the skyrmion dynamics driven by the spin-Hall effect. In particular, to get further fundamental understandings, we perform deterministic simulations where we are able to control the breathing mode of the skyrmion – that in real samples can be due to thermal fluctuations and/or disorder - and therefore we can qualitatively show the effect of such thermal modes on the skyrmion dynamics. We also build up a generalized Thiele equation and introduce an experiment to validate our findings.

We have finally shown, in the second topic, the results carryied out on antiferromagnets. We have worked on modeling antiferromagnets by means of a micromagnetic formalism. We

have studied the fundamental properties of the model both in term of resonance response and self-oscillation. We have investigated the AFM resonance as a function of the homogeneous intersublattice exchange. We have also executed a ferromagnetic resonance studies, the results indicates that the ferromagnetic resonance frequency coincides with the frequency of the self-oscillation at the critical current. In particular, we also focused on the analytical derivation of the expression of modes of antiferromagnetic order in easy plane and easy axis materials. The antiferromagnet acoustic mode is only shown because the optical mode exists in some specific conditions. In addition, we have worked on the synthesis and the characterization of microparticles of manganese (II) oxide to study its magnetic properties.

ACKNOWLEDGEMENTS

I can't forget my colleagues and best friends who have shared me all moments, happy and sad. They were my second family who encourage me and push me up. Big thanks for you all: Meryem Chelly, Dr. Fatima Sayed, Nadine Hammoud, Alaa Tafech, Joanna akrouche, Rim Faraj, Rosario Emanuele Cilla ,Giusy Mistretta, Giuseppe Poerio, Valentina Torregrossa, Yostina George, Federico Casella, Monica Reigia Blanco, Dr. Julieta Puig, Lisandra de Castro Alves, Manuel Gonzalez Gomez, Nerea Borja, Dario de la Iglesia Rodriguez, Iria Rodràiguez Arias, Dr. Jose Manuel Blanco and all whom I have met through these three years and left a great touch deep inside my soul.

To Meryem I would like to say that I was so lucky that life has given me a person who have become close to me as myself! This person is you. We have endured exile together, worked sometimes together, laughed together, and even cried together. Thank you a lot my dear friend, my dear sister.

To all of the doctors who helped get me to where I am today, thank you. Thanks to all my doctors to whom I owe what I have reached today.

The another great merit goes back to my family, my mother, my brothers Mohammad and Ali, and my lovely sister Walaa, whom without their support and prayers I would not have achieved this great rank. I owe you my presence and achievements. Thanking you would not express the enormous amount of gratitude that I have towards you.

I have experienced the most beautiful moments, memories that will stay engraved in my mind and my heart as ever I last. These moments, whether easy or hard, have taught me great lessons that will always push me forward through my social as well as practical life.

Finally, the words of thanks are always difficult to express and remain helpless of describing my gratitude to all those people.

❖ *To my great parents whom I will never have enough chances to say Thank You.*

❖ *To my mother for her ongoing love and support and to my father who could not see this thesis completed. As you look down from heaven, I hope you're proud of your little girl.*

❖ *To all my family and to those who had sacrificed their lives for the dignity of human being, the world peace, and the pursuit of truth.*

I would love to dedicate my work for you.......

"The gift of mental power comes from God, Divine Being, and if we concentrate our minds on that truth, we become in tune with this power"
Nicola Tesla

Contents

List of Abbreviations

CMOS   Complementary Metal transistors Oxide Semiconductor

GMR   Giant Magnetoresistance

AP   Antiparallel;

STT   Spin-Transfer-Torque;

OOP   Out-Of-Plane;

IP   In-Plane;

MTJ   Magnetic Tunnel Junction;

LLG   Landau-Lifshitz-Gilbert;

LLGS   Landau-Lifshitz-Gilbert-Slonczewski;

DW   Domain-Wall;

VCMA   Voltage Controlled Magnetocrystalline Anisotropy;

SOC   Spin-Orbit Coupling;

SHE   Spin-Hall Effect;

AMR   Anisotropic Magnetoresistance;

AHE   Anomalous Hall Effect;

DMI   Dzyaloshinskii-Moriya Interaction;

HM   Heavy Metal;

FM   Ferromagnetic;

IDMI   Interfacial Dzyaloshinskii-Moriya Interaction;

BC   Boundary conditions

IEC   Interlayer Exchange Coupling

SOT   Spin-Orbit Torque;

SHA   Skyrmion Hall Angle

AFM   Antiferromagnet

FLT   Field like Torque

DLT   Damping Like Torque

FMR   Ferromagnetic Resonance;

LL   Landau-Lifshitz;

THZ   Terahertz

AFMR   Antiferromagnetic Resonance

AHSO   AFM-based Oscillators

TDS   Time-Domain THz Spectroscopy

DC   Direct Current

MnO   Manganese (II) oxide

SEM   Scanning Electron Microscopy

TEM   Transmission Electron Microscopy

XRPD   X ray powder diffraction

SQUID   Superconducting Quantum Interference Device Magnetometer System

VSM   Vibrating Sample Magnetometry

ZFC   Zero Field Cool

FC   Field Cool

XRD   X ray diffraction

JCPDS   Joint Committee on Powder Diffraction Standards

List of Symbols

dV	volume of magnetic material;
r	vector position;
M	magnetization vector;
M_S	saturation magnetization;
μ_i	spin angular momentum;
m	normalized magnetization vector;
ε_{ex}	exchange energy density;
A	exchange constant;
mx	x-component of the normalized magnetization;
my	y-component of the normalized magnetization;
mz	z-component of the normalized magnetization;
ε_{an}	uniaxial anisotropy energy density;
k_1 or k_u	first order uniaxial anisotropy constant;
k_2	second order uniaxial anisotropy constant;
k_3	third order uniaxial anisotropy constant;
u$_k$	unit vector of the magnetization easy axis;
Hm	magnetostatic field;
μ_0	vacuum permeability
n	normal unit vector;
ε_m	magnetostatic energy density;
Nx	x-axis shape-dependent demagnetizing factor;
Ny	y-axis shape-dependent demagnetizing factor;
Nz	z-axis shape-dependent demagnetizing factor;
H$_{ext}$	external magnetic field;
ε_{ext}	external magnetic field energy density;
ε_{tot}	total energy density of a ferromagnetic body;
H$_{eff}$	effective field;
h$_{eff}$	normalized effective field
T	material temperature;
ξ	three-dimensional white Gaussian noise;
τ	torque;
L	orbital angular momentum;
γ	gyromagnetic ratio;
G	Landé factor;
e	electron charge;
m_e	electron mass;
μ_B	Bohr magneton;
$\hbar$	Planck's constant;
α	damping parameter or Gilbert damping;
j$_{FE\text{-}oop}$ or J	perpendicular current density;
J_{MTJ}	perpendicular current density in MTJ;
m$_p$	normalized magnetization of the pinned layer;
m	normalized magnetization of the free layer;

$\boldsymbol{\tau}_{\mathbf{oop}}$	STT in OOP device;
t or t_{FE}	thickness of the ferromagnet;
$\varepsilon\left(\mathbf{m},\mathbf{m_p}\right)$	polarization function;
$\varepsilon_{SV}\left(\mathbf{m},\mathbf{m_p}\right)$	polarization function for spin-valve;
η	spin polarization factor for OOP device;
$\varepsilon_{MTJ}\left(\mathbf{m},\mathbf{m_p}\right)$	polarization function for MTJ;
$d\tau$	dimensionless time step
$\mathbf{j_{FE\text{-}ip}}$ or j_{FE}	IP current density through ferromagnet;
τ_{IP}^{a}	adiabatic torque for IP device;
P	spin polarization factor for IP device;
τ_{IP}^{na}	non-adiabatic torque for IP device;
β	non-adiabatic parameter;
$\Delta \mathrm{H}_{k\perp}$	perpendicular anisotropy field;
$Vapp$	applied voltage;
H_{SO}	Spin-orbit Hamiltonian;
$V\left(\mathbf{r}\right)$	electrical potential;
$\boldsymbol{\tau}_{\mathbf{SHE}}$	SHE torque;
θ	spin-Hall angle;
j_{HM}	charge current density through a HM;
j_{s}	spin current;
$\varepsilon_{bulkDMI}$	bulk DMI energy density;
D	DMI parameter;
$\varepsilon_{\mathrm{InterDMI}}$	interfacial DMI energy density;
ξ	DMI characteristic length;
S	skyrmion number;
A	exchange constant;
α_{G}	Gilbert damping;
A^{ex}	interlayer exchange coupling (IEC) constant;
$\varepsilon_{tot}^{L,U}$	total micromagnetic energy density; superscripts L and U refer to lower and upper FMs;
ε^{ex}	interlayer exchange energy;
t_{RU}	thickness of the Ru layer;
D^{L}	refers to the lower FM;
D^{U}	refers to the upper FM;
$\hat{z}$	unit vector along the z-direction;
μ_0	vacuum permeability;

$\mathbf{H}_m$	magnetostatic dipolar field;
$\mathbf{N}$	unit vector normal to the surface;
θ_{SH}^{L}	spin-Hall angles for the lower FMs;
θ_{SH}^{U}	spin-Hall angles for the upper FMs;
$\mathbf{h}_{th}$	deterministic effective magnetic field;
K_B	Boltzmann constant;
ΔV	volume of the computational cubic cell;
Δt	simulation time step;
T	temperature of the sample;
χ	three-dimensional white Gaussian noise;
γ_0	gyromagnetic ratio;
v	coefficient linking the magnitude of the FLT to the one of the DLT;
j_p	ac current density;
J_{APM}	current amplitude;
Q	topological charge;
$\mathbf{v}$	drift velocity;
$\overset{\leftrightarrow}{\mathcal{D}}$	dissipative tensor;
$\overset{\leftrightarrow}{\mathcal{R}}$	in-plane rotation matrix;
$\langle m \rangle$	average normalized magnetization;
ϕ_0	azimuthal angle;
$\mathbf{F}$	force" resulting from the in-plane external field;
J	exchange integral;
$\hat{S}_i$	spins of the ith adjacent magnetic ions;
$\hat{S}_j$	spins of the jth adjacent magnetic ions;
β_1	anisotropy coefficient
$\mathbf{h}_{ani\text{-}1}$, $\mathbf{h}_{ani\text{-}2}$	uniaxial anisotropy field for sublattices 1 and 2, respectively;
ω_0	AFM resonance

j	direction of the electric currents
A_{AFM}	homogeneous intersublattice exchange constant
$A_{AFM\text{-}NH}$	non-homogenous intersublattice exchange constant
a	atomic lattice constant
J_{OFF}	elimination current
J_{ON}	ignition current
$K\alpha$	radiation
λ	wave length
θ_B	bragg angle
λ_{Cu}	wave length of copper
(h,k,l)	miller index
χ^{-1}	inverse of the magnetic susceptibility
χ	magnetic susceptibility
C	material-specific Curie constant
T	absolute temperature
T_c	curie temperature

List of Figures

List of Tables

1 Chapter 1

Introduction

Conventional electronics depends on the transport of charges in materials semiconductors (Si), based on the use of Complementary Metal transistors Oxide Semiconductor (CMOS). The branch of condensed matter physics studies the store and process data thus rely on the manipulation of electronic charges. Spotlight today that the using of the spin of the electron come into sight as one of the best candidates [1] for the improvement of post-electronics CMOS.

Spintronic is a field full of developments in which advantages on magnetic storage can be achieved. For more details, as we know, the electron has many properties including charge and spin. The spin and the charge of the electron were used separately until the twentieth century. Since a few decades, they are studied and used together in a field of Spintronics. This branch of condensed matter physics studies how the magnetization vector is influenced by a charge current, and, vice versa, how the change of the magnetization vector can affect the charge current. The foundation of Spintronics is in 1998 by A. Fert and P. Grunberg [2] as being the discovery giant magnetoresistance (GMR). This magnetoresistive effect allows to generate two levels of resistance depending on the relative orientation of two magnetic layers F (parallel or antiparallel) separated by a non-magnetic layer N. It is possible to change the magnetization and the resistance of a system composed of F/N/F by the application of a magnetic field or a spin-polarized current. This option paves the way for the development of devices such as magnetic the read-heads of magnetic hard disks.

A radical change in the field of spintronics appeared by the discovery of spin transfer phenomena, which was theoretically assumed by Berger [3] in 1977 and then highlighted by J.C.Slonczewski [4] and Berger [5]. This phenomenon is based on the conservation of the global kinetic moment of a system. When a charge current consisting of electrons spin passes through a ferromagnetic material, the spin current (kinetic moment) is transferred to the magnetization of the material, generating a torque on the latter. Note that the applied current makes it possible to move a magnetic domain wall [6] [7] or a skyrmion [8] [9], more specifically to reverse the magnetization of material [10] [11] [12], or to maintain ferromagnetic precession [13][14].

The urgent need to generate spin currents lead to the generation of new branch of spintronics: spin-orbitronics. A promising method to create spin currents consist in using materials with a strong spin-orbit coupling (SOC) proposed by D'yakonov and Perel in 1971 [15]. Note that the spin currents are amortized over short distances [16] in such materials.

My thesis is focused on the use of spin currents generated by spin-orbit interactions to move magnetic skyrmions and excite self-oscillations and resonance dynamics in antiferromagnetic materials.

1.1 Thesis overview

This thesis is structured as follows:

Chapter 2 shows the several aspects concerning Micromagnetics, Spintronics, in order to provide the fundamental background necessary to read the results of this thesis. First, a short introduction on the micromagnetic formalism and the torques acting onto the magnetization vector of a ferromagnetic material have been presented. We also explain the key concepts of Spin-Orbitronics.

Chapter 3 presents the theoretical concepts and the results of the simulations behind skyrmions. Briefly we summarize the properties of skyrmions, a review of topology and skyrmion number is given, followed by a thorough discussion of the theoretical investigations on magnetic skyrmion dynamics in ferromagnetic materials. The latter is made of two main parts: the first one on skyrmions based random bit generator and the second one on micromagnetic understanding of the skyrmion Hall angle current dependence in perpendicular magnetized ferromagnets.

Chapter 4 addresses the discussion of the results obtained on antiferromagnets (AFM). First of all, we have introduced the antiferromagnetic material and their common properties. We then present the micromagnetic modeling of antiferromagnets. We spotlight on the modes of antiferromagnetic resonance (acoustic mode) by the means of calculations. Finally, further studies direct towards the understanding of THz oscillators based on antiferromagnets, and show the model of the devices and the results obtained.

Chapter 5 deals with the experimental part regarding microparticles of Manganese (II) oxide, overarching the synthesis and the characterization techniques owed to analyse the samples. In the last part, we show the results obtained for the microparticles of MnO and we present a discussion compared to MnO nanoparticles and finally conclusions.

2 Fundamentals

This chapter covers the fundamentals concerning micromagnetism. That one is divided into 4 Sections. Primarily, a brief introduction of the micromagnetic formalism (section 2.1) and the torques acting onto the magnetization vector of a ferromagnetic material (section 2.2) will be presented. Section 2.3 will deal with the key concepts of Spin-Orbitronics.

2.1 Micromagnetism

Micromagnetism aims to investigate the static and dynamical properties of ferromagnetic particles at a mesoscopic level [17][18][19]. In 1935, Landau and Lifshitz [20][21] study the structure of a wall between two antiparallel (AP) domains, and continues with Brown [22][23]and many others up the present time. For several centuries, Micromagnetism have been studied and the main object of is the nucleation processes of domains, domain structures properties [24]. Notice that the concept of nucleation was introduced by Brown [24].

A key assumption of micromagnetism is that the magnetization is the magnetic moment per unit volume, designed by the vector position **r**, can be represented as a vector **M**, and has a modulus M_S constant in time (M_S is the saturation magnetization of the material). The direction of M varies continuously with the coordinates x, y, and z. Particularly, the size of the volume has to be chosen large enough in order to contain a sufficient number n of magnetic momenta μ_i ; on the other side, small enough to allow for the magnetization to easily change between each volume element (Fig. 2.1). The magnetization of a magnetic material with n atoms per unit volume is:

$$\mathbf{M}(\mathbf{r},t) = \frac{\sum_{i=1}^{n} \boldsymbol{\mu}_i}{dV} \qquad (2.1)$$

The magnetization vector can be expressed in terms of the unit vector $\mathbf{m}(\mathbf{r},t) = \mathbf{M}(\mathbf{r},t)/M_S$. (Notting that both notations m(**r**,t), **M**(**r**,t) or **m** and **M** will be used to indicate the magnetization).

In particular, the fundamental energetic contributions, known as standard micromagnetic energies plays an important role in the equilibrium configurations of the magnetization **M.**
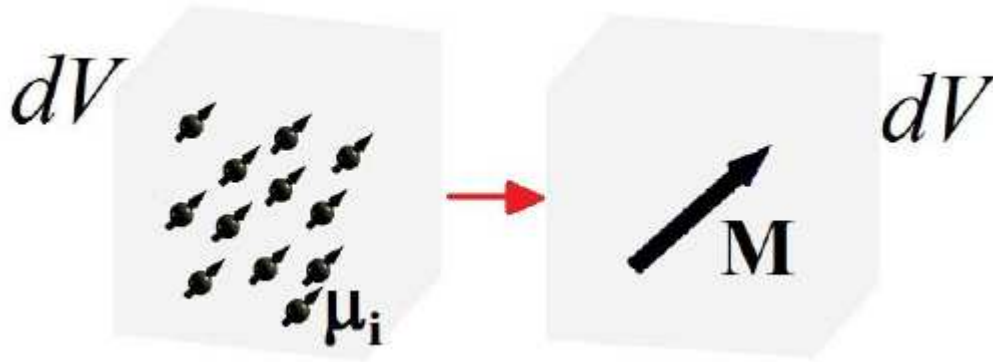
Fig. 2.1: fundamental assumption of Micromagnetics, by which the magnetic momenta μ_i

of a volume element *dV* can be represented by a magnetization vector **M** .

2.1.1 Exchange energy

The exchange energy has a purely quantum mechanical origin, and obtained from the competition between the Coulomb's interaction and the principle of exclusion of Pauli. Specifically, the exchange is a short-range interaction which tends to align the magnetic moment of the spin in the same direction [17] [23]. The volume energy density ε_{ex} related to the exchange is:

$$\varepsilon_{ex} = A[(\nabla m_x)^2 + (\nabla m_y)^2 + (\nabla m_z)^2] \tag{2.2}$$

being *mx*, *my*, and *mz* the three normalized components of the magnetization along the three spatial coordinates *x*, *y*, and *z*, respectively, and *A* is the exchange constant in J/m.

2.1.2 Uniaxial Anisotropy energy

The anisotropy energy arises in crystalline lattices, the energy is lower for magnetisation parallel to certain crystallographic directions: these are labelled easy axes of magnetisation, against hard axes of magnetisation [17] [23]. The volume energy density ε_{an} related to the uniaxial anisotropy is:

$$\varepsilon_{an} = k_1 \sin^2 \theta + k_2 \sin^4 \theta + k_3 \sin^6 \theta + ... \tag{2.3}$$

where k_1, k_2 and k_3 are uniaxial anisotropy constants expressed in J/m³ and θ is the angle between the magnetization direction and the easy axis. Mostly, only the first term is take into account, leading to:

$$\varepsilon_{an} = k_1 \left[1 - \left(\mathbf{m}.\mathbf{u}_k \right)^2 \right] \tag{2.4}$$

being $\mathbf{u}_k$ the unit vector of the easy axis. For $k_1 > 0$ ($k_1 < 0$) the axis is called easy (hard) axis since the magnetic moments will prefer to orient collinear (perpendicular) to it in order to reduce the anisotropy energy.

2.1.3 Magnetostatic energy

The magnetostatic energy is associated to the interactions between the magnetic dipoles inside the material [17]. The magnetic field related with this energy is called demagnetizing field $\mathbf{H_m}$ (or dipole field inside the material). The magnetostatic energy of a uniformly magnetized ferromagnetic material of magnetization M is defined according to [25] by:

$$\varepsilon_m = -\frac{1}{2}\mu_0 \mathbf{M}.\mathbf{H_m} \tag{2.5}$$

The factor $\frac{1}{2}$ is introduced in order to avoid counting twice the interaction between couples of magnetic moments.

The magnetostatic energy rely upon the geometrical properties of the ferromagnet as:

$$\mathbf{H_m} = -M_s \left(N_x m_x \hat{x} + N_y m_y \hat{y} + N_z m_z \hat{z} \right) \tag{2.6}$$

where N_x, N_y, N_z are the shape-dependent demagnetizing factors along the x, y, z directions, respectively. For a sphere, the three demagnetizing factors are equal, $N_x=N_y=N_z=1/3$ (for symmetry reasons) and there is no favoured direction that minimizes the magnetostatic energy. For an infinitely long cylinder along the z direction $N_z = 0$ while $N_x = N_y = \frac{1}{2}$, hence the magnetization favours to lie along the axis of the cylinder.

2.1.4 Zeeman energy

Zeeman energy corresponds to the interaction between the magnetization and the external magnetic field H_{ext}. Its energy density ε_{ext} can be written as [17] [23]:

$$\varepsilon_{ext} = -\mu_0 \mathbf{M}.\mathbf{H_{ext}} \tag{2.7}$$

2.2 Equilibrium and dynamical equations

The previous energetic contribution plays an important role in the equilibrium configuration of the magnetization. Indeed, each contribution support different energetic minima and the final equilibrium state is obtained by the balance between them.

Therefore, the total energy of a generic ferromagnetic body is given by:

$$\varepsilon_{tot} = \varepsilon_{ex} + \varepsilon_{an} + \varepsilon_{m} + \varepsilon_{ext} = A\left[\left(\nabla m_x\right)^2 + \left(\nabla m_y\right)^2 + \left(\nabla m_z\right)^2 +\right] +$$
$$k_1\left(1 - \left(\mathbf{m}.\mathbf{u_k}\right)^2\right) - \frac{1}{2}\mu_0 \mathbf{M}.\mathbf{H_m} - \mu_0 \mathbf{M}.\mathbf{H_{ext}} \tag{2.8}$$

Based on a variational calculus, the effective field [23] can be defined as the functional derivative of the total energy density:

$$\mathbf{H_{eff}} = -\frac{1}{\mu_0 M_S}\frac{\delta \varepsilon_{tot}}{\delta \mathbf{m}} \tag{2.9}$$

where the functional derivative is expressed by:

$$\frac{\delta}{\delta \mathbf{m}} = \frac{\partial}{\partial \mathbf{m}} - \nabla.\frac{\partial}{\partial\left(\nabla \mathbf{m}\right)} \tag{2.10}$$

Hence, the total effective field is given by:

$$\mathbf{H_{eff}} = -\frac{2A}{\mu_0 M_S}\left(\nabla^2 \mathbf{m}\right) - \frac{2k_1}{\mu_0 M_S}\left(\mathbf{m}.\mathbf{u_k}\right)\mathbf{u_k} + \mathbf{H_m} + \mathbf{H_{ext}} \tag{2.11}$$

2.2.1 Dynamical equation

The dynamics of magnetization is governed by the Landau-Lifschitz equation [20] which is given by:

$$\frac{d\mathbf{M}}{dt} = -\mu_0\gamma\left(\mathbf{M}\times\mathbf{H_{eff}}\right) - \frac{\mu_0\gamma\alpha}{M_S}\mathbf{M}\times\left(\mathbf{M}\times\mathbf{H_{eff}}\right) \tag{2.12}$$

Then, it is reformulated by Gilbert [26][27]in the form:

$$\frac{d\mathbf{M}}{dt} = -\mu_0 \gamma (\mathbf{M} \times \mathbf{H}_{\text{eff}}) + \frac{\alpha}{M_S} \left(\mathbf{M} \times \frac{d\mathbf{M}}{dt} \right) \tag{2.13}$$

where γ is the gyromagnetic ratio, expressed by: $\gamma = -\frac{ge}{2m_e} = -\frac{g\mu_B}{\hbar}$ in A.m^{-1}.s^{-1} being g the Landé factor [28][29], e and m_e the charge and the mass of the electron, respectively, μ_B the Bohr magneton and $\hbar$ the Planck's constant. $\gamma = (1+\alpha^2)\gamma$, α the damping term without dimensions, $\mathbf{M}$ the magnetization in A.m^{-1}, M_S the magnetization saturation in A.m^{-1}, $\mathbf{H}_{\text{eff}}$ the effective filed in A.m^{-1}. These two formulations are analytically equivalent, but the first equation is more suitable for numerical calculations, because of the explicit expression of the time derivative of the magnetization.

The first term of this equation is the precessional term. It design a persistently movement of rotation of the magnetization vector around its equilibrium position (see Fig. 2.2(a)). This rotation is caused by a perturbation of the magnetic field inside the material. The second term of Landau-Lifschitz of the equation describes the damping. This term is purely phenomenological. In fact, the amplitude of the oscillations of a spin decrease over time to allow magnetization to join the equilibrium position (see Fig. 2.2(b)). Without this term the magnetization would rotate indefinitely.
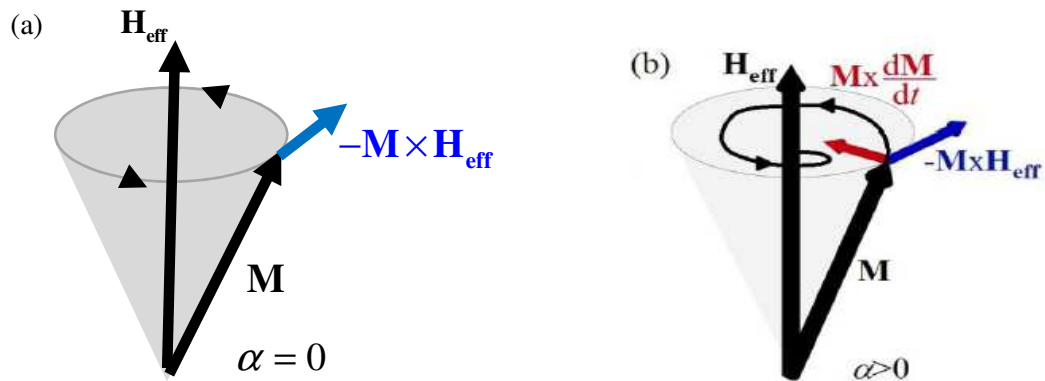
Fig. 2.2: (a) persistent precession of the magnetization $\mathbf{M}$ around the effective field $\mathbf{H}_{\text{eff}}$ when only the conservative torque acts. (b) damped precession of the magnetization when the damping torque is take in account.

2.2.2 Spin-Transfer Torque

Spin-Transfer Torque (STT) effect was first theoretically studied by Slonczewski [4] and Berger [5] in 1996; where the electrons flowing through a magnetic layer are spin polarized along the magnetization of F1 (see Fig. 2.3).

When these spin-polarized electrons pass through another magnetic layer (F2), the polarization direction may have to change depending on the relative orientation of F1 and F2. So, the thick layer filters the spin component in the opposite direction that called reflected spins, and the homologue with the same direction goes through it. As a result, the spin angular momentum of the current is changed to the direction of the magnetization. Due to the conservation of angular momentum, the loss of angular momentum of the current in the interface is absorbed by the thin layer, and thus this layer receives a torque. The torque acting on the magnetization due to spin transfer and depends on the current density J.

Part of the entering spins in the ferromagnet1 are polarized in the same direction of M_1, generating the spin-polarized current, which will transfer a spin-torque onto the magnetization M_2 of the adjacent ferromagnet2. Part of the entering spins is reflected with a polarization opposite to.

In addition, two types of STT can be take into account. The first one acts when the current flows perpendicularly to the plane of a multilayer [4] that arises in out-of-plane (OOP) devices. The second one is exerted when the current flow is in-plane (IP) [5] that arises in IP devices.
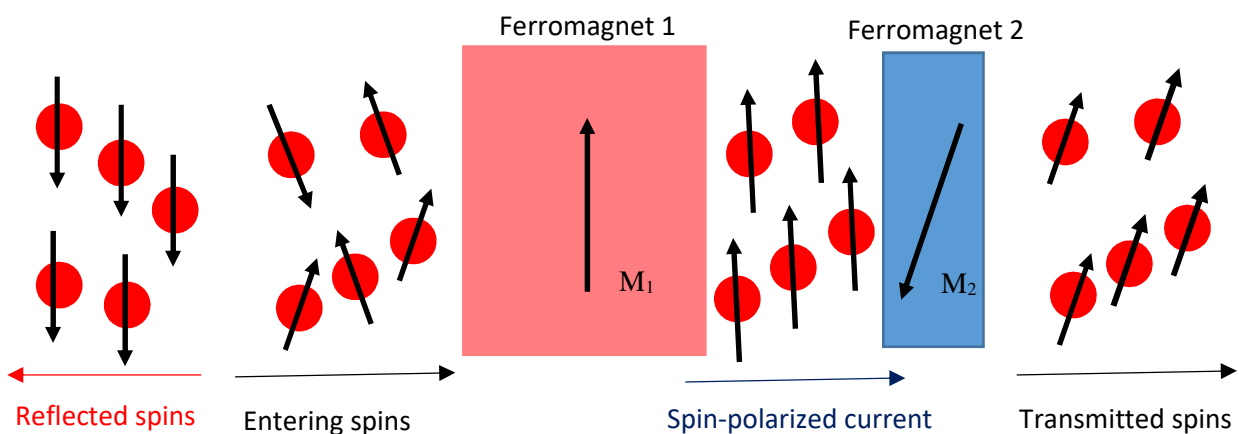
Fig. 2.3: a simplified illustration of spin transfer torque process, ferromagnet 1 and ferromagnet 2 refers to ferromagnetic film with magnetization M_1 and M_2 respectively. The thick magnetic layer is used to produce a polarized electric current which in turns produces a torque on M_2.

2.2.3 STT in OOP devices

For understanding the behavior of spin transfer torque in OOP devices, the structure consists of two magnetic layers separated by a thin non-magnetic layer.

Commonly, the device consists of a thick ferromagnet where the magnetization direction is fixed, in order to produce a spin-polarized current, and it is called *pinned* or *fixed* or *reference layer* or *polarizer* as well. The other ferromganet is thinner to allow changes of its orientation and it is called free *layer* [16]. From chemical point of view, the spacer layer can either be a *spin valve* (the spacer is an electrical conductor) or a magnetic tunnel junction (MTJ) (the spacer is an electrical insulator). By passing an electrical current density $\mathbf{j_{FE\text{-}oop}}$ perpendicularly to the device through the pinned layer $\mathbf{m_p}$, one can produce a spin-polarized current and, thus it control the magnetization $\mathbf{m}$ of the free layer, via STT $\boldsymbol{\tau}_{oop}$ (see Fig. 2.4(a)), which can be designed as an additional contribution to the LLG equation, as derived by Slonczewski [4]:

$$\boldsymbol{\tau}_{oop} = \frac{g\mu_B \mathbf{j_{FE\text{-}oop}}}{\gamma_0 e M_s^2 t}\varepsilon\left(\mathbf{m},\mathbf{m_p}\right)\left[\mathbf{m}\times\left(\mathbf{m}\times\mathbf{m_p}\right)\right] \tag{2.14}$$

being t the thickness of the free layer and $\varepsilon\left(\mathbf{m},\mathbf{m_p}\right)$ the polarization function, whose expression related to the relative orientation between the pinned and free layer magnetization, Specially, for spin-valves the following $\varepsilon\left(\mathbf{m},\mathbf{m_p}\right)$ expression is usually given by [14]:

$$\varepsilon_{SV}\left(\mathbf{m},\mathbf{m_p}\right) = \left(-4 + \left(1+\eta\right)^3 \frac{\left[3+\left(\mathbf{m.m_p}\right)\right]}{4\eta^{3/2}}\right)^{-1} \tag{2.15}$$

where η is the spin polarization factor related to the magnetic material. Whereas, the expression for MTJ becomes [30]:

$$\varepsilon_{MTJ}\left(\mathbf{m},\mathbf{m_p}\right) = \frac{0.5\eta}{\left[1+\eta^2\left(\mathbf{m.m_p}\right)\right]} \tag{2.16}$$

Now, it is worth noting that the Slonczewski torque acts as an anti-damping torque [31]. In fact, by looking at the damping torque in Eq. (2.12) and (2.13), with the STT expression in Eq. (2.31), it is reasonable to note that they have a similar vector structure.

Finally, the dimensionless *Landau-Lifshitz-Gilbert-Slonczewski (LLGS) equation* for a spin valve reads:

$$\frac{d\mathbf{m}}{d\tau} = -\left(\mathbf{m} \times \mathbf{h}_{\text{eff}}\right) + \alpha\left(\mathbf{m} \times \frac{d\mathbf{m}}{d\tau}\right) +$$
$$\frac{g\mu_B \mathbf{j}_{\text{FE-oop}}}{\gamma_0 e M_s^2 t} \varepsilon_{SV}\left(\mathbf{m}, \mathbf{m_p}\right)\left[\mathbf{m} \times \left(\mathbf{m} \times \mathbf{m_p}\right)\right]$$

(2.17)

where the dimensionless time step $d\tau = \gamma_0 M_s dt$ has been introduced.

Then as well, the LLGS for an MTJ is obtained:

$$\left(1 + \alpha^2\right)\frac{d\mathbf{m}}{d\tau} = -\left(\mathbf{m} \times \mathbf{h}_{\text{eff}}\right) - \alpha\left(\mathbf{m} \times \left(\mathbf{m} \times \mathbf{h}_{\text{eff}}\right)\right) -$$
$$\frac{g\mu_B \mathbf{j}_{\text{FE-oop}}}{\gamma_0 e M_s^2 t} \varepsilon_{MTJ}\left(\mathbf{m}, \mathbf{m_p}\right)\left[\mathbf{m} \times \left(\mathbf{m} \times \mathbf{m_p}\right) - q(V)\left(\mathbf{m} \times \mathbf{m_p}\right)\right]$$

(2.18)

Where, by comparing the last two equations the main difference is the presence of "field like torque" or "out-of-plane" torque $q(V)\left(\mathbf{m} \times \mathbf{m_p}\right)$ (an additional component of the STT term).
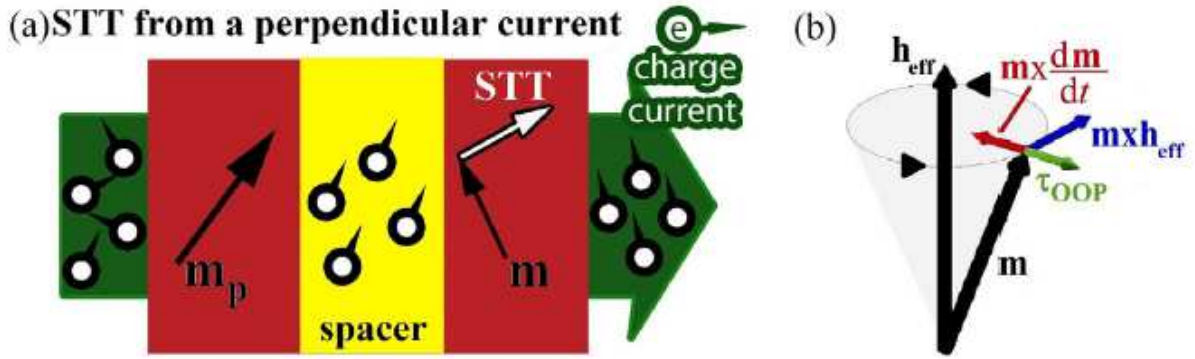
Fig. 2.4: (a) schematic illustration of the spin-transfer torque exerted on the free layer magnetization in an OOP device. (b) representation of all the torques acting on the magnetization.

2.2.4 STT in IP devices

An IP device can be visualized as a ferromagnetic wire that characterised by a length much larger than its width, containing two different magnetic regions separated by DWs (see Fig. 2.5). By generating an electrical current density $\mathbf{j}_{\text{FE-ip}}$ through the strip, the current is naturally polarized and can produce a distortion motion of DWs (translation of the domains). More specifically, the electron spin is approximately parallel to the local magnetization and any modification in the spin direction induces a STT which shifts the DW along the wire length.

Berger reformulated the expression of the *adiabatic* STT τ_{IP}^{a} in the form [5]:

$$\tau_{IP}^{a} = \frac{\mu_B P}{\gamma_0 e M_s^2} \left(\mathbf{j}_{\text{FE-ip}}.\nabla \right) \mathbf{m} \tag{2.19}$$

being *P* the spin polarization factor, which represents the amount of spins polarized by the local magnetization.
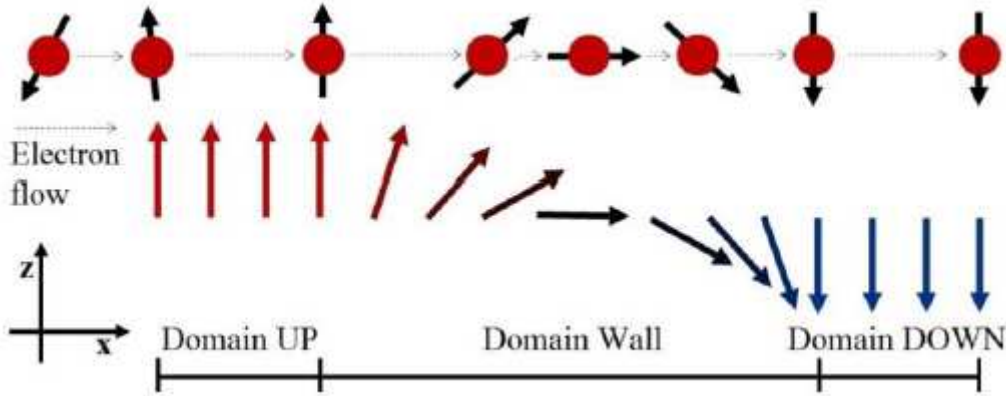
Fig. 2.5: schematic representation of two domains (UP and DOWN) separated by a domain wall. A non-polarized electron flowing through this magnetization configuration will change the direction of its spin adiabatically, namely it will follow the local magnetization orientation.

Then, a non-adiabatic STT was phenomenologically added in order to describe an experimental results and its expression is:

$$\tau_{IP}^{na} = -\frac{\mu_B P}{\gamma_0 e M_s^2} \beta \left(\mathbf{j}_{\text{FE-ip}}.\nabla \right) \mathbf{m} \tag{2.20}$$

where β is the non-adiabatic parameter. We can be found in [33] the physical origin of the two mentioned torques.

Taking into account the adiabatic and non-adiabatic STT, the dimensionless LLG equation for IP devices is:

$$\frac{d\mathbf{m}}{d\tau} = -\left(\mathbf{m} \times \mathbf{h}_{\text{eff}} \right) + \alpha \left(\mathbf{m} \times \frac{d\mathbf{m}}{d\tau} \right) +$$
$$\frac{\mu_B P}{\gamma_0 e M_s^2} \left(\mathbf{j}_{\text{FE-ip}}.\nabla \right) \mathbf{m} - \frac{\mu_B P}{\gamma_0 e M_s^2} \beta \left(\mathbf{j}_{\text{FE-ip}}.\nabla \right) \mathbf{m} \tag{2.21}$$

2.2.5 Voltage controlled magnetocrystalline anisotropy (VCMA)

The magnetic anisotropy of a ferromagnet and its magnetization can feel a variations by the application of an electric field [34][35]. There are two main reasons for the ferromagnet to be ultrathin: i) its perpendicular anisotropy has to extract from interfacial effects [36], ii) the electric field can only invade few monolayers of the ferromagnet. Hence, in MTJ (thick free layers >3 nm) the VCMA has not been observed. This phenomenon arises from the electric field which influences the spins of the ferromagnetic layer, afterwards, affects the perpendicular anisotropy [37]. In MTJs composed of an iron rich CoFeB and a MgO spacer, the VCMA is performed as a linear change of the perpendicular anisotropy effective field with respect to the applied voltage (see Fig 2.6). Specifically, the variation of the perpendicular anisotropy field $\Delta H_{k\perp}$ with the applied voltage V_{app} has been measured where, $\Delta H_{k\perp} = H_{k\perp}(V_{app}) - H_{k\perp}(0)$ being $H_{k\perp}(V_{app})$ and $H_{k\perp}(0)$ the perpendicular anisotropy field values with and without the applied voltage, respectively. The relation is linear with a slope of 0.6 kOe/V [34].
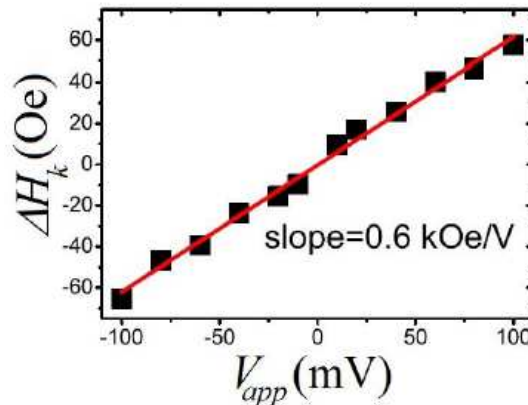
Fig. 2.6: variation of the effective perpendicular anisotropy field when a voltage is applied in CoFeB-MgO MTJs [34].

2.3 Spin-orbit interactions

A novel direction of Spintronics - that can be named spin-orbitronics – exploits the Spin-Orbit Coupling (SOC). The latter can be designed by the coupling between the spin angular momentum of an electron and the orbital one in non-magnetic materials that can be involved to manipulate the magnetization of a ferromagnet [12][38][39][40][41].

To simply understand the bases of the spin-orbit coupling (SOC), the approximated expression of its Hamiltonian *HSO* is given by:

$$\mathbf{H}_{SO} \approx \lambda \mathbf{L}.\boldsymbol{\mu} \tag{2.22}$$

where λ is a parameter that depends on the electrical potential *V* "seen" by the electron. It is well known that for the heavy metals (HMs) (Platinum, Tantalum, Iridium, Palladium, Tungsten, etc.) are usually characterized by a large SOC.

The SOC has two distinct origins: an intrinsic and an extrinsic. The extrinsic effect has two contributions: the "skew-scattering" (oblique diffusion) and the "side-jump". The "skew-scattering" corresponds to the diffusion of an electron of conduction by an impurity. When the electron arrives near an impurity, it feels the electric field radiated by it (see Fig. 2.7(a)) which results in a magnetic field. The spin of this electron couples to this magnetic field and generates an inelastic diffusion of the electron on the impurity. The "side-jump" mechanism involves a wave packet arriving on an impurity. Electron orbitals constituent this wave packet are deformed near the electric field radiated by impurity via spin-orbit coupling. This results in a shift of the centre of gravity of the wave packet associated with each spin component in a direction perpendicular to the pulse variation (see Fig. 2.7(b)) [42].
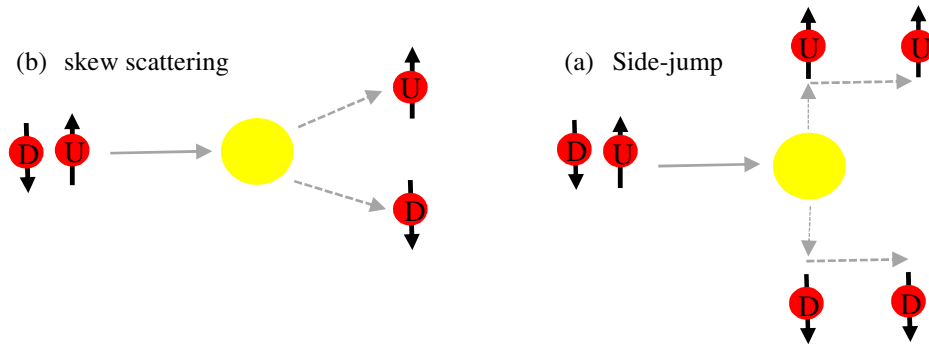
Fig. 2.7: Schematic picture of (a) the skew scattering mechanism and (b) the side-jump mechanism. The letters U and D refer to the sign of the spin, respectively spin-UP and spin-DOWN. The yellow circle represents an impurity.

The intrinsic effect derives from the properties of the band structures of the material [43]. This effect also does not depend explicitly on impurities. The deviation of spins does not take place only on the impurities but in all the material for the electrons of the band of conduction. Kontani et al. have proposed a model for the intrinsic spin Hall effect [44], which is based on the work of Karplus and Luttinger [45].

Extrinsic and intrinsic SOC are involved for the generation of spin-orbit associated phenomena, such as the anisotropic magnetoresistance (AMR), the spin-Hall effect (SHE), the anomalous Hall effect (AHE), and the Dzyaloshinskii-Moriya Interaction (DMI).

In the following subparagraphs, the micromagnetic model of the SHE and DMI will be described.

2.3.1 Spin-Hall Effect

The Spin Hall Effect was predicted theoretically by Dyakonov and Perel in 1971 [46]. The Spin Hall Effect originates from the coupling of the charge and spin currents due to spin-orbit interaction where an ultrathin ferromagnetic layer is coupled to HM layer and the charge current flows through the HM (see Fig. 2.8).
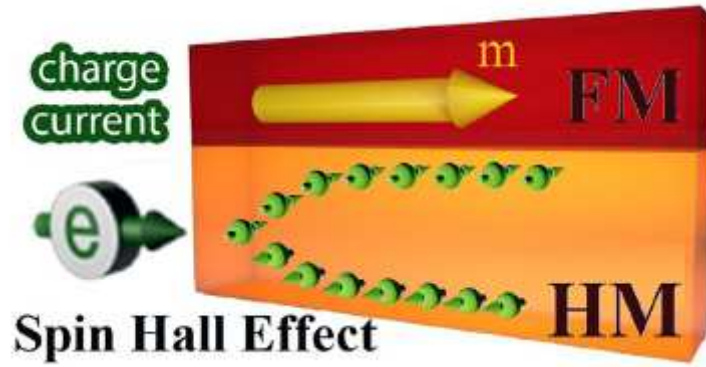
Fig. 2.8: schematic picture of the FM/HM bilayer, where the SHE arises, inducing opposite spin accumulations near the upper and lower surface of the HM.

A spin-current is generated from the charge current j_{HM} because of the spin-dependent scattering in the HM, which create a spin accumulation of opposite sign at the upper and lower surface of the HM (the charge current is along the x axis, the spin-polarization is along the y-axis). A vertical spin-current is generated and then absorbed by the FM, exerting a torque τ_{SHE} on its magnetization, which is given by the following relation:

$$\boldsymbol{\tau}_{\mathbf{SHE}} = -\frac{g\mu_B\theta_{SH}}{2\gamma_0 eM_S^2 t}\mathbf{m}\times\mathbf{m}(\hat{z}\times\mathbf{j}_{HM}) \tag{2.23}$$

being θ_{SH} the spin-Hall angle, which represents the amount of charge current j_{HM} converted

into spin-current j_s: $j_s = \theta_{SH}\, j_{HM}$. $\hat{z}$ is the unit vector in the OOP direction.

It is possible to note that the difference between this torque and the Slonczewski torque of Eq. (2.31) [12][40][41], in which they are similar, is that instead of considering the direction of the

spin-polarization given by the magnetization $\mathbf{m_p}$, here the cross product $(\hat{z} \times \mathbf{j}_{HM})$ indicates the direction of the spin-polarization. Therefore, we can consider that the SHE torque act as an anti-damping term [31].

2.3.2 Dzyaloshinskii-Moriya Interaction

The Dzyaloshinskii-Moriya interaction is an interaction between two neighbouring spins with an atom with large spin orbit coupling.

In fact, while the exchange aimed to align adjacent spins in parallel in order to obtain a uniform magnetization state, the DMI prefers to align them orthogonally, enhancing the formation of rotational magnetization textures. We can classified two types of this interaction; the DMI in bulk material and at the interface of an ultrathin film. Starting with The bulk DMI which is due to a break of the crystal inversion symmetry and the presence of high spin–orbit coupling atoms in a ferromagnetic material (see Fig. 2.9(a)) while the interfacial DMI (*i*-DMI) has its origin in the interfaces of a multilayer, where a thin ferromagnetic material is coupled to a large spin–orbit coupling material (see Fig. 2.9(b)). The energy density for the two types of DMI is expressed by the following way [47]:

$$\varepsilon_{bulkDMI} = D\mathbf{m}.\nabla \times \mathbf{m}$$

$$\varepsilon_{\text{InterDMI}} = D\left[m_z \nabla.\mathbf{m} - (\mathbf{m}.\nabla)m_z\right]$$

(2.24)

D being the parameter taking into account the intensity of the DMI. Indeed, for the expression of $\varepsilon_{interDMI}$,we assume $\dfrac{\partial \mathbf{m}}{\partial z} = 0$.
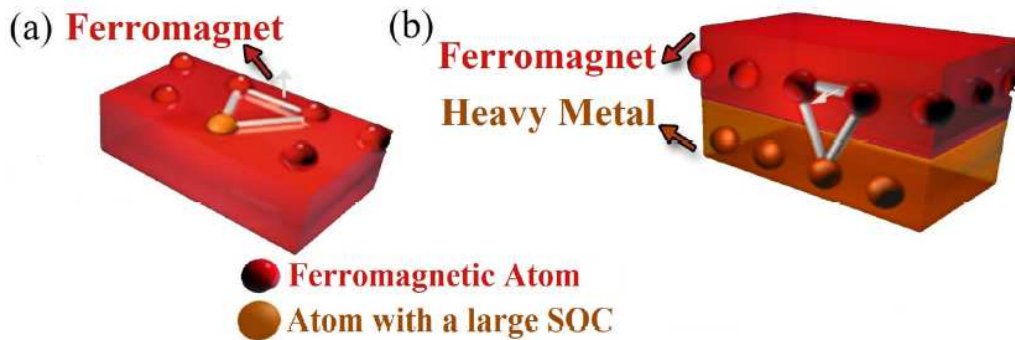
Fig. 2.9: (a) Bulk DMI vector (white arrow) originating in a non-centrosymmetric crystal because of the interaction of the ferromagnetic atoms with an impurity with large SOC. (b) Interfacial DMI vector (white arrow) in a FM/HM bilayer.

Afterwards, the expression of the dimensionless DMI fields:

$$\mathbf{h}_{bulkDMI} = -\frac{1}{\mu_0 M_s}\frac{\delta\varepsilon_{bulkDMI}}{\partial\mathbf{m}} = -\frac{2D}{\mu_0 M_s}\nabla\times\mathbf{m}$$

$$\mathbf{h}_{InterDMI} = -\frac{1}{\mu_0 M_s}\frac{\delta\varepsilon_{bulkDMI}}{\partial\mathbf{m}} = -\frac{2D}{\mu_0 M_s}\nabla\times\mathbf{m}$$

(1.25)

The DMI also affects the boundary conditions (BC) of the ferromagnet as shown in the following equations [47]:

$$\text{Bulk DMI BC: } \frac{d\mathbf{m}}{dn} = \frac{\mathbf{m}\times\mathbf{n}}{\xi}$$

(2.26)

$$\text{Interfecial DMI BC: } \frac{d\mathbf{m}}{dn} = \frac{1}{\xi}(\hat{z}\times\mathbf{n})\times\mathbf{m}$$

where $\xi = \frac{2A}{D}$ is a characteristic length and A is the exchange constant.

The DMI is a fundamental interaction for stabilizing a magnetic skyrmion which will be explained in the next paragraph.

3 Magnetic Skyrmion

The third chapter concerns the study of magnetic skyrmions. Section 3.1 deals with topology of the magnetic skyrmion and shows its different configurations. Section 3.2 is divided into two main parts. The first part (section 3.2.1.1) shows a brief description of the state of the art of the magnetic skyrmion and the results obtained about skyrmion based random bit Generator (section 3.2.1.3). In the section 2.2.2, a brief review on the control of the Skyrmion Hall Angle is presented, followed by the outcomes achieved on Micromagnetic understanding of the skyrmion Hall angle current dependence in perpendicular magnetized ferromagnets

3. Magnetic skyrmions

Magnetic skyrmions are chiral spin textures with a whirling configuration forming in thin ferromagnets. Skyrmions are topologically and relatively energetically stable structures, in comparison with, for example, magnetic vortices or bubbles, because the skyrmion structure cannot be continuously deformed to a ferromagnetic or other magnetic states. For this reason, they have found widespread regions in fundamental and technological part, and a tremendous scientific interest to investigate the magnetic skyrmions theoretically and experimentally. They can be considered a magnetic soliton like as DWs, vortexes and bubbles and they can behave like a rigid object. The name "skyrmion", has been borrowed from the context of particle physics by the physicist Tony Skyrme [48], and then has been transferred to Spintronics.

3.1 Topology and skyrmion number

The term "topologically protected" connect to the classification of magnetic solitons which is characterised by a *skyrmion number S*, defined as [49][50][51]:

$$S = \frac{1}{4\pi} \int \mathbf{m}.\left(\partial_x \mathbf{m} \times \partial_y \mathbf{m}\right) dx dy \qquad (3.1)$$

Generally, the skyrmion number connect to the total variation of the magnetization angle when moving counterclockwise around a circle, divided by 2π [51]. For instance, let's consider the spin configurations in Fig. 3.1. In the first Fig. 3.1(a) the skyrmion number is zero because there is no change in the magnetization angle. Actually, the magnetization angle covers $\pi/2$ in

a counterclockwise sense, after a quarter of turn, if we begin to move from the circled spin. In the later quarter of turn, the magnetization covers again an angle of $\pi/2$ in the clockwise sense, deriving in a zero angle variation with the respect to the starting spin. The same happens for the other consecutive half turn. In Fig. 3.1(b), the skyrmion number equal to 1 due to an observation of 2π continuous rotation of the magnetization angle in a complete turn. In the last Fig. 3.1(c), the skyrmion number equal to 2 as the magnetization covers continuously an angle of 4π in a turn.
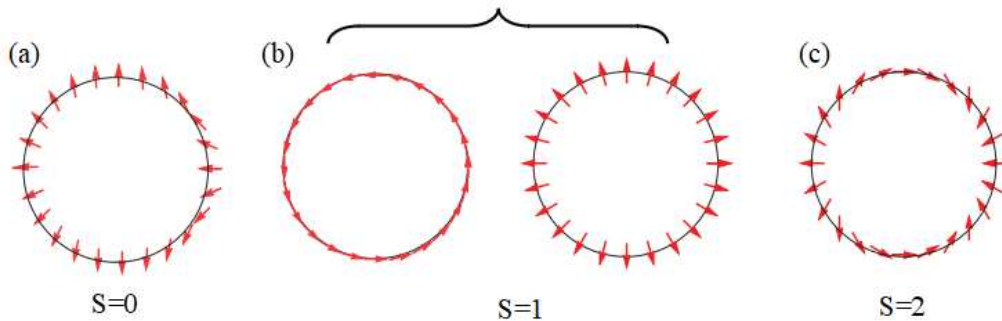
Fig. 3.1: magnetization configurations with skyrmion number *S* equal to (a) zero, (b) one, and (c) two [51].

It is worthy to underline, that DWs have a zero skyrmion number [52], vortexes have $S = \pm 1/2$ [53], and Bubbles characterised by $S = \pm 1$ are called either *Bubble skyrmions*, if stabilized in absence of the DMI and by a competition between exchange and magnetostatic field, or Skyrmions in presence of DMI. Indeed, the quadripole is related to S =2 [54].

Two main characteristics are taken into account in order to nucleate a skyrmion: the first is the application of ferromagnetic materials with the magnetization pointing in the OOP direction and the existence of the DMI. Particularly, two types of skyrmions can be stabilized in the existence of two types of DMI (As explained in subparagraph 2.3.2). The DMI in bulk material stabilize *Bloch skyrmions*, characterized by a vortex like configuration of the domain wall spins (see Fig. 3.2(a)); while in the i-DMI, *Néel skyrmions* are obtained which have a radial distribution of the domain wall spins (see Fig. 3.2(b)) [55] Hence, the sign of the DMI parameter plays an important role in the chirality of the two types of skyrmions. It is necessary to underline that the skyrmion has a double protection due to the energetic minimum and the topology.
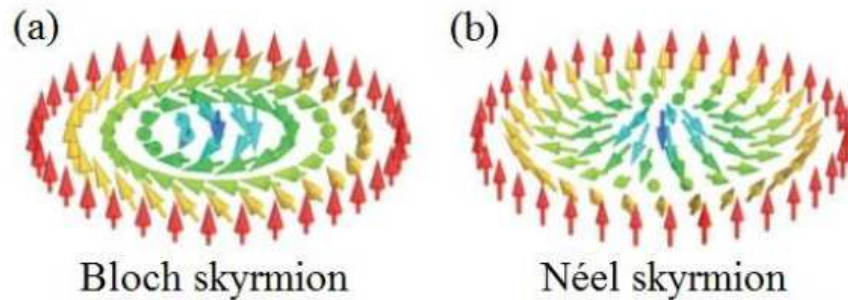
Fig. 3.2 : magnetization distribution of a (a) Bloch skyrmion and (b) Néel skyrmion [55].

The skyrmion, proposed in the context of particle physics [48], has been stabilized in magnetic materials [56] [57]. Magnetic skyrmions range in sizes from 10 nm to approximately 1000 nm depending on material parameters and they are defined by a long lifetime. They can be created and annihilated by spin currents and magnetic fields, and they can be easily moved by an electrical current [56] [57] [58] [59] [60] [61]. Skyrmions are also chiral, which means the skyrmion has a definite "sense of rotation". In other words, the skyrmion and its mirror image cannot be brought to coincide with each other by translation and rotation. The stability of magnetic skyrmions is generally associated to the presence of the DMI (see Section 2.3.2 in chapter 2). Some of new research have recently emerged which includes new materials systems conformist to the category of B20 compounds that host Bloch skyrmions, while in multilayered heterostructures Néel skyrmions can be stabilized [57].

The skyrmions have large mobility under spin-polarized current, which also can contribute to the generation of single skyrmion [63]. Skyrmion motion can be driven by the spin-transfer torque (STT) [9][64] from an in-plane current flowing in the ferromagnets [33], or, more efficiently [9] [64], by the SOT due to the spin-Hall effect (SHE) [38] and to the inverse spin-Galvanic effect [88], originated from a current flowing via a heavy metal with large spin-orbit coupling in contact with a ferromagnet (see Section 2.2.4 and 2.3.1 in chapter 2). The skyrmion shifting is characterized by an in-plane angle with respect to the direction of the applied current, i.e. the skyrmion Hall angle (SHA) [89][90][91].

The control of the SHA is crucial for racetrack memory applications where skyrmions, coding the information, would be inevitably driven towards the sample edges where they could either bounce back or be annihilated. This aspect also limits the maximum applicable current and hence the maximum velocity achievable for the skyrmion. One strategy to overcome this issue is to suppress the SHA by balancing the Magnus force in two coupled skyrmions with opposite topological charge resulting in zero net topological charge, in ferrimagnets [92], synthetic antiferromagnets [93][94], or AFM [95].

Skyrmion detection have been noticed both by means of neutron scattering in momentum space and by the Lorentz transmission electron microscopy in the real space [60], as well as

electrically by a magnetic tunnel junction read-head [66].

The magnetic skyrmions have found widespread applications potential in information storage (memory) due to their interesting properties: small size, stability, individual creation and annihilation as well as facile movement with low current. In fact, the most promising technological applications of skyrmion is in racetrack memory [67], where the presence of a skyrmion code the bit "1", while its absence code the bit "0" [64]. However, several further uses of skyrmion has been predicted, such as in microwave oscillator and detectors [68] [69] [70] [71], or in logic gates [71].

3.2 Investigations on magnetic skyrmion dynamics in ferromagnetic materials

In this paragraph, two main results will be described: the first one on skyrmion based random bit Generator, the second one on the understanding of the skyrmion Hall angle current dependence in perpendicular magnetized ferromagnets.

3.2.1 Skyrmion based random bit Generator

3.2.1.1 Introduction

A random bit generator is a system whose output consists of fully unpredictable (i.e., statistically independent and unbiased) bits [72]. Generally, the output of random bit generator is given in binary form at any time. We can distinct two main types of random bit generators: i) the first one aimed to capture random proceedings in the truly world to generate its sequences. It is designed as truly random bit generators, because in normal case it is impossible for anyone to prospect the next number in the sequences. ii) the second one anticipates that the unpredictable outputs of algorithms are adequate to satisfied the necessity of randomness. It is referred to as pseudo-random generators, because in the real world each value set on based off the system's state [72].

Here, we show the proof of concept of a random bit generator based on magnetic skyrmions by means of micromagnetic simulations. We take advantage of the stochastic behavior of skyrmions in presence of thermal fluctuations to achieve the generation of random bits which is represented by the skyrmion. Principally, we control the skyrmion motion by the SHE in a synthetic antiferromagentic (SAF) device [73] composed of one input branch and two output branches. We use a SAF system because of the zero skyrmion Hall angle. The skyrmions are continuously nucleated in the input branch, shifted by the SHE and at the end divided randomly in the two output branches. Our results pave the way for the

design of a new application of skyrmions as well as of a new generation of random bit generators.

3.2.1.2 Device and Modeling

The computational studies concern micromagnetic simulations of a multilayered nanowire with two output branches (see Fig. 3.3(a)). It is composed of a 3 nm thick Platinum heavy metal (HM) (lower HM) with on top two perpendicular CoNi ferromagnetic layer (FMs) separated by a thin Ruthenium (Ru), layer designed to provide an antiferromagnetic exchange coupling [73] (see Fig. 3.3(a)), and a second HM on top of the whole stack (upper HM) [73].

The device is 1900 nm long and the width of the input and output branches are 320 nm. The thickness of both ferromagnets and Ru layer is 0.8 nm. The physical parameters of CoNi layers taken from [74] [75] , and equal for both ferromagnets, are: saturation magnetization Ms = 600 kA/m, exchange constant A = 20 pJ/m, and damping α_G = 0.1. The value of saturation magnetization is typically obtained by considering hysteresis loops [76] [77] [78] [79] of the ferromagnet. The interlayer exchange coupling (IEC) constant A^{ex} is fixed to -5.0x10^4 J/m^2 [74] [75]. We use a discretization cell of 4x4x0.8 nm^3, and introduce a Cartesian coordinate system with the x-, y- and z-axes lying along the length, the width and the thickness of the device, respectively (see inset Fig. 3.3(a)). The numerical study is carried out by means of a self-implemented micromagnetic solver (it includes the SHE, IDMI and IEC) and post-processing tools [65] [80] [81] [82].

The total micromagnetic energy density of the system under investigation is (the superscripts L and U refer to lower and upper FMs):

$$\varepsilon_{tot}^{L,U} = A(\nabla \mathbf{m})^2 + \varepsilon^{ex} + D^{L,U} \left[m_z^{L,U} \nabla \mathbf{m}^{L,U} - (\mathbf{m}^{L,U} \nabla) m_z^{L,U} \right]$$
$$-k_u \left(\mathbf{m}^{L,U} \cdot \hat{z} \right)^2 - \frac{1}{2} \mu_0 M_s \mathbf{m}^{L,U} \cdot \mathbf{H}_m^{L,U}$$

(3.2)

where m_x, m_y and m_z are the x-, y-, and z-components of the normalized magnetization $\mathbf{m}$, respectively. The interlayer exchange energy is given by $\varepsilon^{ex} = -\frac{A^{ex}}{t_{RU}} (\mathbf{m}^L \cdot \mathbf{m}^U)$ (same contribution for both FMs), where t_{RU} is the thickness of the Ru layer [83]. D is the parameter taking into account the intensity of the IDMI. More specifically, D^L (D^U) refers to the lower (upper) FM. According to our definition, D^L and D^U are the properties of materials (they are not related to the multilayer geometry), i.e. in the specific case where both lower (HM/FM) and upper (FM/HM) interfaces are the same (see inset Fig. 3.3(a)), one would have $D^L = D^U$. We fixed $D^L = D^U = 2.5$ mJ/m^2 [73].

The Pt/FM interface produces the lower IDMI, while the upper IDMI derives mainly from an upper HM. $\hat{z}$ is the unit vector along the z-direction, μ_0 is the vacuum permeability. $\mathbf{H}_m$ is the magnetostatic dipolar field, which is computed by considering both ferromagnetic layers. The boundary conditions related to the IDMI are $\dfrac{d\mathbf{m}^{L,U}}{dn^{L,U}} = \dfrac{1}{\xi^{L,U}}\left(\hat{z}\times\mathbf{n}^{L,U}\right)\times\mathbf{m}^{L,U}$ [84], [64], where $\mathbf{n}$ is the unit vector normal to the surface and $\xi^{L,U} = \dfrac{2A}{D^{L,U}}$ is a characteristic length.

We wish to underline that, when considering the dynamical analysis, the presence of two HMs gives rise to a lower and upper SHE when an electric current is passed through them (the electrical current here denotes a flow of electrons). In order to model this behavior, it is necessary to introduce two spin-Hall angles, θ_{SH}^L and θ_{SH}^U, for the lower and upper FMs, respectively (see inset Fig, 3.3(a)). As for D^L and D^U, according to our definition, the two spin-Hall angles are only linked to material properties. We fixed $\theta_{SH}^L = \theta_{SH}^U = 0.10$ [83].
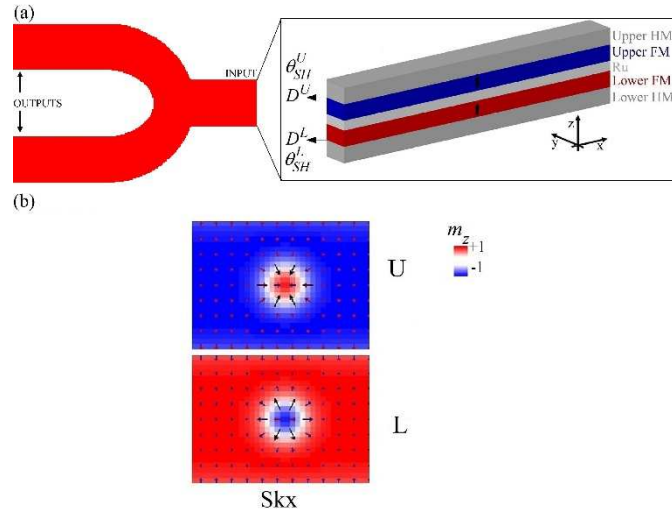
Fig. 3.3: (a) 2D view of the SAF multilayer under investigation, where the input branch and two output branches are indicated. Inset: 3D sketch of the input branch, where the ferromagnets (FM), separated by a Ru layer, are sandwiched between different heavy metals (HM). (b) Snapshot representing examples of the spatial distribution of the magnetization for SAF Néel skyrmion (Skx). A color scale, linked to the z-component of the magnetization, is also indicated.

The thermal effects are accounted into the micromagnetic solver as a stochastic term $\mathbf{h}_{th}$ added to the deterministic effective magnetic field in each computational cell $\mathbf{h}_{th} = \left(\chi/M_S\right)\sqrt{2\left(\alpha K_B T / \mu_0 \gamma_0 \Delta V M_s \Delta t\right)}$, with K_B being the Boltzmann constant, ΔV the volume of the computational cubic cell, Δt the simulation time step, T temperature of the sample, and

χ a three-dimensional white Gaussian noise with zero mean and unit variance [85].

3.2.1.3 Results

We perform a micromagnetic study at room temperature T=300 K and zero external field. We apply an electrical current j_{HM} only though the lower HM, and we calculate the current distribution, which is the same for the two output branches and equal to the half of the one in the input branch. All the results are shown for $j_{HM} = -2.0 \times 10^8$ A/cm^2, but identical results are realized for current densities in the range -2.25×10^8 A/cm$^2 \le j_{HM} \le -0.25 \times 10^8$ A/cm^2. We carry out micromagnetic simulations within a simulation time of 60 ns, where we continuously nucleate a single Néel skyrmion in the input branch. In order to simulate such a periodic nucleation, we adjusted our micromagnetic code such that, every 5 ns, a skyrmion is nucleated in the input branch.

First, we carry out sistematic simulations to proper design the perpendicular anisotropy. We observe that if the perpendicular anisotropy is low enough, when the skyrmion arrives at the intersection, it becomes elongated through the two output branches (Fig. 3.4(a)). This is an undesired result, because it would not make our device work correctly. Therefore, we need to properly design the value of the perpendicular anisotropy constant. In fact, if we increase perpendicular anisotropy constant ku to 0.50 MJ/m^3, the skyrmion remains localized and goes to one of the two output branches. Differently from the zero-temperature case, here the selection of the output branch is stochastic due to the presence of thermal fluctuations [66], which lead to different bit generations (Figs. 3.4(b), (c) and (d), Fig.3.5).
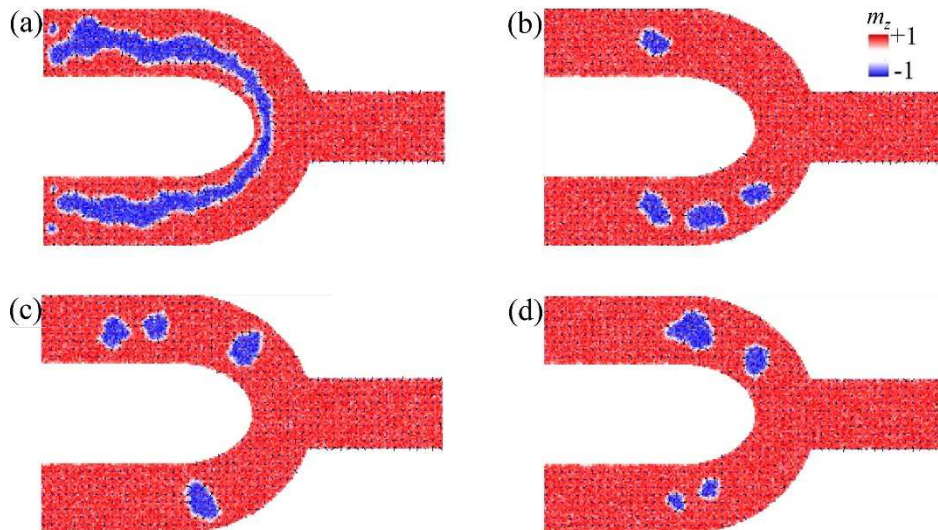
Fig. 3.4: Spatial distribution of the magnetization when (a) the perpendicular anisotropy constant is lower than 0.50 MJ/m^3, and for (b), (c) and (d) different skyrmion combinations when ku=0.50 MJ/m^3.
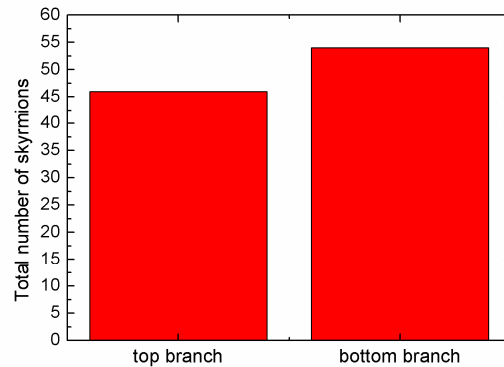
Fig. 3.5: The Statistics on how many skyrmions goes up (Top branch) and down (bottom branch). This shows that skyrmions are almost equally divided into the two output branches.

3.2.1.4 Conclusion

In summary, a full micromagnetic simulations show the possibility to move randomly skyrmions in presence of spin-Hall effect and thermal fluctuations in a synthetic antiferromagnets, where the skyrmion hall effect is absent. We have detected that, under the steady action of the current, skyrmions stochastically divided in the two output branches of our device starting from a continuous nucleation in the input branches. Our results are also robust to the presence of defects in the form of randomly distributed grains of the perpendicular anisotropy. Our achievements open the path for the design of random bit generators based on skyrmions.

3.2.2 Micromagnetic understanding of the skyrmion Hall angle current dependence in perpendicular magnetized ferromagnets.

To study the skyrmion stability, we refer to a nonlinear ansatz [86] that can be used to investigate the stability of the skyrmion by studying the magnetic parameter as a function of the external field and temperature. In addition, it has been also shown that the thermal effects induce: internal distortions of the skyrmion, which then loses its circular symmetry [86], expansion and shrinking of the skyrmion core (thermal breathing mode), and a thermal drift [87](gyrotropic motion).

Recent experimental observations have shown a current dependence of the SHA. Jiang *et al.* [89] attributed such dependence to the presence of random pinning potentials in their materials. Basically, at low currents in the so-called creep regime, the skyrmion motion is strongly affected by pinning from defects and its SHA is current-dependent. Whereas, at high

currents skyrmion is characterized by a steady-flow regime where its SHA is independent of the current. Differently, Litzius *et al.* [90], claimed that the current dependence of the SHA results from the combination of the SHE-field-like torque (FLT) [95] and the internal deformations of the skyrmion. In order to add our contribution to this debate, we performed micromagnetic simulations where FLT and the damping like torque (DLT) are simultaneously applied to a breathing skyrmion. Our results show the qualitative picture that fundamentally explains the current dependent SHA.

3.2.2.1 Micromagnetic Model

We analyze a square sample where a thin ferromagnetic layer is in contact with a Platinum underlayer in order to obtain the IDMI and SHE.

The micromagnetic study is performed by means of state-of-the-art processing tools and home-made micromagnetic solver GPMagnet [97][98] which numerically integrates the Landau-Lifshitz-Gilbert-Slonczewski equation by applying the time solver scheme Adams-Bashforth, where the SHE-FLT and SHE-DLT are taken into account:

$$\frac{d\mathbf{m}}{d\tau} = -(\mathbf{m} \times \mathbf{h_{eff}}) - \alpha\left(\mathbf{m} \times \frac{d\mathbf{m}}{d\tau}\right)$$
$$-d_j\left[\mathbf{m} \times (\mathbf{m} \times (\hat{\mathbf{z}} \times \mathbf{j_{HM}}))\right] - \nu d_j\left(\mathbf{m} \times (\hat{\mathbf{z}} \times \mathbf{j_{HM}})\right) \tag{3.3}$$

Where $\mathbf{m} = \mathbf{M}/M_s$ is the normalized magnetization of the ferromagnet, $\tau = \gamma_0 M_s t$ and is the dimensionless time, with γ_0 being the gyromagnetic ratio, and M_s the saturation magnetization.

$\mathbf{h_{eff}}$ is the normalized effective field, which includes the exchange, IDMI, magnetostatic, anisotropy and external fields. α is the Gilbert damping. $d_j = \dfrac{g\mu_B\theta_{SH}}{2\gamma_0 eM_S^2 t_{FM}}$ where g is the Landé factor, μ_B is the Bohr magneton, θ_{SH} is the spin-Hall angle, e is the electron charge, t_{FM} is the thickness of the ferromagnetic layer. $\hat{\mathbf{z}}$ is the unit vector along the out-of-plane direction, and $\mathbf{j_{HM}}$ is the electrical current density flowing into the Pt heavy metal which gives rise to the SHE. ν is a coefficient linking the magnitude of the FLT to the one of the DLT [96].

The lateral dimension of the square sample under investigation is $1.6\,\mu m$, while the ferromagnet thickness is $t_{FM} = 1$ nm. The discretization cell used in the simulations is

2.0x2.0x1.0 nm^3. We introduce a Cartesian coordinate system with the x- and y- axes lying into the plane of the sample, whereas the z-axis is oriented along the out-of-plane direction. We consider typical parameters for CoFeB/Pt bilayers [64]: M_S=1000 kA/m, exchange constant A=20 pJ/m, perpendicular anisotropy constant k_u=0.80 MJ/m3, D=2.0 mJ/m^2, α =0.03, and $\theta_{SH} = 0.1$. The current j_{HM} flows in the x-direction, thus the spin-current inside the heavy metal is polarized along the y-direction. We apply an out-of-plane external field H_z=25 mT in all the simulations to have a metastable skyrmion [86] and to reduce the transient breathing mode. The SHE-FLT has the direction of the spin-polarization (y-axis). In order to deeply understand the role of the SHE-FLT and the physics underlying the SHA current dependence, we consider, in the first part, a constant FLT, while, in the second part, we fix the DLT and we change the FLT.

For stochastic simulations, the thermal fluctuations are added to the deterministic effective magnetic field as a random term in each computational $\mathbf{h}_{th} = (\chi / M_S)\sqrt{2(\alpha K_B T / \mu_0 \gamma_0 \Delta V M_s \Delta t)}$, with K_B being the Boltzmann constant, ΔV the volume of the computational cubic cell, Δt the simulation time step, T temperature of the sample, and χ a three-dimensional white Gaussian noise with zero mean and unit variance [23][99]. The noise is assumed to be uncorrelated for each computational cell.

3.2.2.2 Results

Study of the skyrmion Hall angle

We have shown that thermal fluctuations excite non-stationary breathing modes. It is also well known that disorder physical parameters can give rise to a continuous change of the skyrmion size [100], hence we conclude that the non-stationary breathing mode should have a role in the explanation of the current dependence SHA found in the experiments [89][90]. In addition, it has been already shown that the combination of an in-plane field and a breathing mode induces a Bloch skyrmion shift [101]. With this in mind, we have designed a numerical experiment to investigate the dynamical properties of a breathing Néel skyrmion driven by the

FLT and DLT. In order to excite the skyrmion breathing mode by means of an ac perpendicular spin-polarized current (see sketch in Fig. 1.15(a)) to resemble the effect of thermal fluctuations and/or disordered physical parameters, we add to Eq. (3.3) the following STT term [70]:

$$-\frac{g\mu_B j_p}{\gamma_0 e M_S^2 t_{FM}} \varepsilon_{MTJ}\left(\mathbf{m}, \mathbf{m}_p\right)\left[\mathbf{m}\times\left(\mathbf{m}\times\mathbf{m}_p\right)\right] \tag{3.4}$$

where $j_p = J_{AMP} \sin(2\pi f t)$ is the ac current density, J_{APM} with f and being its amplitude and frequency, respectively. $\varepsilon_{MTJ}(\mathbf{m}, \mathbf{m}_p) = \dfrac{2\eta}{\left[1 + \eta^2(\mathbf{m}.\mathbf{m}_p)\right]}$ is the polarization function [20][89], where $\eta = 0.66$ is the spin polarization factor, and $\mathbf{m}_p$ is the magnetization of the polarizer, which is considered fixed along the out-of-plane direction, thus generating a perpendicularly polarized spin-current.

A. *Characterization of the breathing modes*

The skyrmion dynamics in presence of a persistent breathing mode are studied at T=0 K and Hz=25 mT, in order to obtain some simple and fundamental achievements. Fig. 3.6(b) shows the FMR response of the skyrmion, where the peak-to-peak amplitude of $<m_z>$ is plotted as a function of the ac current frequency f. For the range of J_{AMP} plotted, the response is linear with a FMR frequency equal to 2.9 GHz, in qualitative agreement with previous studies [70][100]. However, the presence of Hz introduces an upper threshold for the applied current (in our case is 2.0 MA/cm^2) over which the skyrmion is annihilated for frequencies near the FMR one. This occurs because, during half period of the current, Hz favors the skyrmion shrinking which becomes critical over a certain value of the current amplitude.

For the current-driven dynamics of the skyrmion, to avoid skyrmion annihilation, we consider ac currents with frequencies larger than the FMR one, i.e. GHz, and we will focus on two cases: small breathing mode, where the perpendicular current amplitude J_{AMP} is 2 MA/cm^2, and large breathing mode, with J_{AMP} equal to 6 MA/cm^2 (note that far from the resonant frequency the skyrmion does not annihilate at this current density).
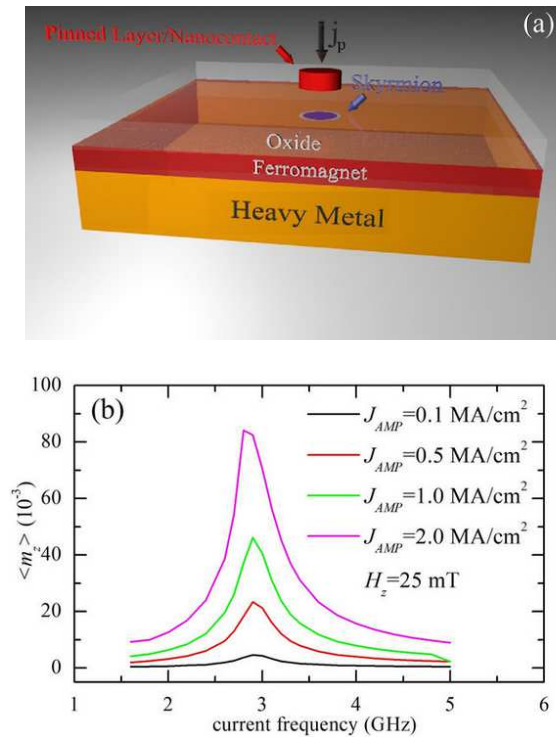
Fig. 3.6: (a) sketch of the device under investigation to study the FMR response of the skyrmion, where the ac perpendicular current is locally injected via a nanocontact. (b) FMR frequency response driven by the ac perpendicular current when H_z=25 mT and T=0 K, for different values of J_{AMP} as indicated in the legend.

B. Effect of the field-like torque

When considering a rigid skyrmion, its motion driven by the DLT is not affected by the FLT. In particular, the role of the FLT is to elongate the skyrmion along the direction of the in-plane field [101][102] leading to a noncircular skyrmion, without modifying the skyrmion velocity and SHA, but only the maximum applicable current. This result is in agreement with previous works on Bloch skyrmions [102]. Figure 3.6 displays such a deformation along the field direction, where the main panel shows the spatial-averaged y-component of the skyrmion magnetization <my_sk> as a function of the in-plane field. As expected, <my_sk> is almost zero at zero field because the skyrmion is symmetric and circular, while it increases linearly with the field. This result is confirmed by the spatial distribution of the skyrmion magnetization (insets in Fig. 3.7), where we can observe how the skyrmion becomes non-circular as the field increases.
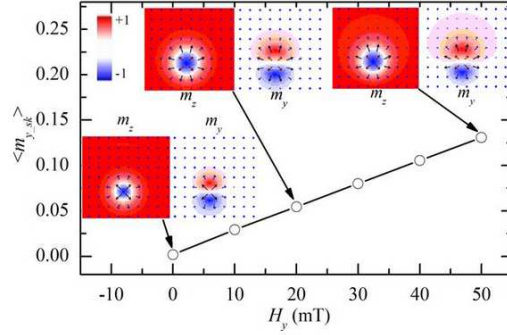
Fig. 3.7: average y-component of the magnetization of the skyrmion as a function of the in-plane field. Inset: spatial distribution of the magnetization displaying the skyrmion for Hy=0 mT, 20 mT and 50 mT. The left panel represents the z-component of the magnetization, while the right panel represents the y-component. The same color scale for both components is also indicated.

We have also investigated the Effect of the breathing mode and the Dynamics driven by SHE-DLT and SHE-FLT in presence of breathing mode in which the results didn't shown here, see this ref. [103].

C. Generalized Thiele's Equation

A generalized Thiele's equation to qualitatively confirm our achievements as well as an experiment to quantify the effect of the FLT.

The effect of the FLT on the skyrmion dynamics can be also analytically demonstrated by including into the Thiele's equation developed in Refs. [101] [104] the DLT due to the SHE. The magnetization distribution of the magnetic Néel skyrmion can be represented in the form $\mathbf{m}(\mathbf{r},t) = \sin\theta(\rho,t)\hat{\rho} + \cos\theta(\rho,t)\hat{z}$ with $\mathbf{r} = (x, y)$ and taking into account a slow dependence on time [Wang et al. PRB(R) **92**, 020403 (2015)]. Hence, the generalized Thiele's equation reads

$$\mathbf{G} \times \mathbf{v} - \alpha \overleftrightarrow{\mathcal{D}} \cdot \mathbf{v} + 4\pi d'_j \overleftrightarrow{\mathcal{R}}\left(\phi_0 = \frac{\pi}{2}\right) \cdot \mathbf{j_{HM}} + \mathbf{F} = 0. \tag{3.5}$$

On the first member, $\mathbf{G}$ is the "gyrocoupling vector" with $\mathbf{G} = -4\pi Q\hat{z}$, $Q = -1$ the topological charge, $\mathbf{v} = \dot{\mathbf{R}}(t)$ ("•" denotes the time derivative and $t = \dfrac{\tau}{\gamma_0 M_s}$ is the time) the drift velocity with , $\mathbf{R} = (X,Y)$ is the skyrmion guiding center experiencing the effect of the in-plane bias field that coincides with the geometric center for a symmetric skyrmion;

$\overleftrightarrow{\mathcal{D}} = \int \left(\frac{\partial \langle \mathbf{m_0} \rangle}{\partial \tilde{r}_\alpha} \cdot \frac{\partial \langle \mathbf{m_0} \rangle}{\partial \tilde{r}_\beta} \right) d\tilde{x} d\tilde{y}$ is the dissipative tensor ($< \ldots >$ denotes the time average over a single period T of the microwave excitation) function of the shape of the skyrmion expressed in terms of the scaled components $\tilde{r}_\alpha(\tilde{r}_\beta) \rightarrow \frac{r_\alpha}{L_{sc}} \left(\frac{r_\beta}{L_{sc}} \right)$ with $\alpha, \beta = x, y$, $d_j' = \gamma_0 M_s d_j L_{sc} I$ with

$I = \frac{1}{4} \int_0^\infty d\tilde{\rho} \left(\sin\theta\cos\theta + \tilde{\rho} \frac{d\theta}{d\tilde{\rho}} \right)$ a dimensionless integral in the dimensionless variable $\tilde{\rho}$ (θ is the polar angle), $\overleftrightarrow{\mathcal{R}}$ is the in-plane rotation matrix depending on the azimuthal angle ϕ_0 [64]. Finally, $\mathbf{F}$ is the "force" resulting from the in-plane external field with

$F_\alpha = -\gamma_0 L_{sc} \int \langle \mathbf{m_0} \rangle \cdot \left(\frac{\partial \langle \mathbf{m_0} \rangle}{\partial \tilde{r}_\alpha} \times \langle \mathbf{m} \times \mathbf{H}_{\text{eff}} \rangle \right) d\tilde{x} d\tilde{y}$ with $\alpha = x, y$, where $\langle \mathbf{m} \rangle = \langle \mathbf{m_0} + \delta\mathbf{m} \rangle$ with $\delta\mathbf{m} \ll \mathbf{m}_0$

the fast time dependent dynamic part $\delta\mathbf{m} \ll \mathbf{m}_0$ [101].

From Eq. (3.5), by following similar calculation as in Ref. [64], we can determine the skyrmion velocity components:

$$\begin{pmatrix} v_x \\ v_y \end{pmatrix} = -d_j' \begin{pmatrix} -\dfrac{\alpha \mathcal{D}}{1+\alpha_G^2 \mathcal{D}^2} & \dfrac{1}{1+\alpha^2 \mathcal{D}^2} \\ -\dfrac{1}{1+\alpha^2 \mathcal{D}^2} & -\dfrac{\alpha \mathcal{D}}{1+\alpha^2 \mathcal{D}^2} \end{pmatrix} \begin{pmatrix} j_{HM} \\ 0 \end{pmatrix} - \begin{pmatrix} -\dfrac{\alpha \mathcal{D}}{1+\alpha^2 \mathcal{D}^2} & \dfrac{1}{1+\alpha^2 \mathcal{D}^2} \\ -\dfrac{1}{1+\alpha^2 \mathcal{D}^2} & -\dfrac{\alpha \mathcal{D}}{1+\alpha^2 \mathcal{D}^2} \end{pmatrix} \begin{pmatrix} \tilde{F}_x \\ \tilde{F}_y \end{pmatrix},$$

with $\mathcal{D} \approx 1$ and $\tilde{F}_\alpha = \dfrac{F_\alpha}{4\pi}$ yielding:

$$\begin{cases} v_x = d_j' \dfrac{\alpha \mathcal{D}}{1+\alpha^2 \mathcal{D}^2} j_{HM} + \dfrac{\alpha \mathcal{D}}{1+\alpha^2 \mathcal{D}^2} \tilde{F}_x - \dfrac{1}{1+\alpha^2 \mathcal{D}^2} \tilde{F}_y, \\ v_y = d_j' \dfrac{1}{1+\alpha^2 \mathcal{D}^2} j_{HM} + \dfrac{1}{1+\alpha^2 \mathcal{D}^2} \tilde{F}_x + \dfrac{\alpha \mathcal{D}}{1+\alpha^2 \mathcal{D}^2} \tilde{F}_y. \end{cases} \tag{3.6}$$

Then, the skyrmion Hall angle can be computed

$$\phi_{SH} = \arctan \left[\frac{d_j' j_{HM} + \alpha \mathcal{D} \tilde{F}_y + \tilde{F}_x}{d_j' \alpha \mathcal{D} j_{HM} + \alpha \mathcal{D} \tilde{F}_x - \tilde{F}_y} \right] \tag{3.7}$$

We note that, at fixed current density j_{HM} , ϕ_{SH} decreases, for example, when the total force increases negatively.

For $j_{HM} = 0$ and for small damping $\alpha \ll 1$, we get $v_x \simeq -\tilde{F}_y$ and $v_y \simeq 0$ (being $\tilde{F}_x$ small) in agreement with Ref. [101]., where $v_x \approx F_y/(4\pi Q)$ with Q = -1. In our analytical study, a negative $\tilde{F}_y$ corresponds to a positive applied field and we obtain that if $F_y < 0$ ($F_y > 0$) we get $v_x > 0$ ($v_x < 0$). In other words, when the DLT is absent, the FLT promotes a prevalent skyrmion motion along the *x*-direction for an applied field along the *y*-direction. This qualitative discussion on the analytical approach is consistent with the micromagnetic simulations shown in Fig. 6 (in this ref. [103]) and with the summary in Table I.

Table I. Summary of the directions of motion of skyrmion under the effect of the different sources. X indicates which source of motion is active. FLT and DLT are considered for positive field and current. [1] See Supplemental Material [105], Movie 3. [2] See Supplemental Material [105], Movie 4.

Breathing mode	FLT	DLT	X direction	Y direction
X			no motion	no motion
	X		no motion	no motion
		X	negative (small)[1]	Negative
X	X		positive	negative (small)
X		X	negative (small)[1]	negative
	X	X	negative (small)[1]	negative
X	X	X	negative/positive depending on DLT and FLT[2]	negative

3.2.2.3 Conclusions

In summary, we have performed a numerical experiment based on micromagnetic simulations to understand the effect of SHE-FLT and DLT on a non-rigid (breathing) skyrmion. We have preliminarily demonstrated that the breathing of the skyrmion can be originated by thermal fluctuations. We have also shown that the SHE-FLT and DLT promote two antagonist

skyrmion motions: the former occurs mainly along the x-axis, while the latter occurs mainly along the y-direction.

Therefore, the combination of the breathing mode and a sufficiently large SHE-FLT gives rise to the current dependence of the SHA, as observed in the experiments [89][90] Our result is qualitatively confirmed by a generalized Thiele's equation and could be confirmed by an experiment, where the SHA should be characterized as a function of an in-plane field for different currents. According to the amplitude of the range where the SHA exhibits the current dependence, it would be possible to estimate the effect of the SHE-FLT.

4

ANTIFERROMAGNETIC DYNAMICS

The main object of this chapter is to discuss the results obtained on antiferromagnets AFM. Section 4.1 introduces the antiferromagnetic material and shows their general properties. Section 4.2 describes the modeling of antiferromagnets, and the state of the art. Section 4.3 deals with the exchange energy in antiferromagnet. Section 4.4 focuses on the modes of antiferromagnetic resonance by the means of calculations. The last section includes an introduction on THz oscillators based on antiferromagnets, describing the model of the device and providing a discussion and conclusion of the results achieved on AFM.

4.1 Antiferromagnetic materials

Many works in recent years have been devoted to the study of physical properties of antiferromagnets (AFM) materials due to their potential applications in information processing and storage. We can identify the following advantages for the use of AFM: i) in the presence of a moderate magnetic fields the antiferromagnetic-coupled moments are not changed, ii) the multiple magnetic configurations are stable in the absence of dipolar interactions, iii) roughly the null wandering fields reduces the interaction among neighbouring elements in the same device, iv) mostly they are characterised by higher magnetic ordering temperature more plentiful in nature than ferromagnets. As long as this list reflects good features, the domain research in antiferromagnet has not seen a large widespread due to the difficulties in manipulating and the probing of their magnetic order. Indeed, in 1970 Louis Neel described during his Nobel lecture that the AFM as "interesting but useless". In the last decades, we have observed the built-in of antiferromagnets based on spintronics [106][107][108]. Presently, it is available to control and detect the antiferromagnetic moment by the means of electric pulses [109].
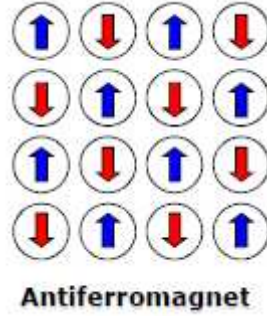
Fig. 4.1: in AFM the magnetic moments of atoms or molecules, align in a regular way with neighbouring spins (on different sublattices) pointing in opposite directions.

4.2 Equation of motion for antiferromagnets

The model of antiferromagnet consists of two sublattices of magnetization $\mathbf{M_1}$ and $\mathbf{M_2}$ oppositely oriented and each of magnitude $\mathbf{M}_s$.

The exchange forces are considered as fields $\mathbf{H_1} = -\lambda\mathbf{M_2}$, $\mathbf{H_2} = -\lambda\mathbf{M_1}$ acting on the sublattices 1 and 2. It is well known that in antiferromagnetic systems there are preferred directions of orientation, and in similarity to ferromagnets, we present an anisotropy energy density constant K to define the energy contributory in wheeling both spin systems relative to the crystal lattice. The anisotropy field for small deflections acting on each sublattice is given by $\mathbf{H}_A = \mathbf{K}/\mathbf{M_S}$. We consider the static field $\mathbf{H_0}$ and the preferred field axis to be in the z-direction. Noting that the demagnetizing effects doesn't take into consideration because we consider that the crystal composed of a single domain (the shape is spherical).

The equation of motion, taking into account the transverse rf field, is given by:

$$\begin{aligned}
\frac{d\mathbf{M_1}}{dt} &= \gamma\mathbf{M_1}\times\left[\left(H^x - \lambda M_2^x\right)\mathbf{i} + \left(H^y - \lambda M_2^y\right)\mathbf{j} + \left(H_0 + H_A + H_E\right)\mathbf{k}\right] \\
\frac{d\mathbf{M_2}}{dt} &= \gamma\mathbf{M_2}\times\left[\left(H^x - \lambda M_1^x\right)\mathbf{i} + \left(H^y - \lambda M_1^y\right)\mathbf{j} + \left(H_0 - H_A - H_E\right)\mathbf{k}\right]
\end{aligned} \tag{4.1}$$

here $\mathbf{H}_E = \lambda M_S = \lambda M_1^z = -\lambda M_2^Z$ Defining $M^- = M_x - jM_y$, $H^- = H_x - jH_y$, we solve for the susceptibility :

$$x^- = M^- / H^- = 2\gamma^2 M_S H_A / (w - w_0)^2 ;$$

$$w_0 / \gamma = H_0 \pm \left[H_A (H_A + 2H_E) \right]^{\frac{1}{2}} .$$

(4.2)

Noting that H_E enters only if $H_A \neq 0$. For $H_0 = 0$ and $H_A \ll H_E$, the zero field splitting is $w_0 \cong \gamma (2H_A H_E)^{\frac{1}{2}} = \gamma (2K\lambda)^{\frac{1}{2}}$. In Eq. (4.2) the two frequencies related to different directions of circular polarization.

In the ordinary antiferromagnetics such as FeO, MnO, MnF_2, Cr_2O_3, we may evaluate $\mathbf{H}_A \sim 10^3$ Oe and $\mathbf{H}_E \sim 10^6$ Oe. After $(2\mathbf{H}_A\mathbf{H}_E) \sim 5 \times 10^4$ Oe and $w_0 \sim 5cm^{-1}$ and if we compare this frequency with the experimental frequency $3cm^{-1}$, we find that $w_0 \sim 5cm^{-1}$ is higher than it exploit by Maxwell [110] et al and Hutchison [111].

4.3 Exchange energies in antiferromagnets

The exchange interaction is the strongest interaction in AFM. On certain suppositions it can be exposed that the energy of interaction of atoms i, j holding electron spins S_i and S_j consists of term:

$$U = -2JS_i.S_j$$

(4.3)

where J is exchange integral, and is connected to the overlap of the charge distributions of the atoms i, j. $\hat{S}_i$ and $\hat{S}_j$ are the spins of the ith and jth adjacent magnetic ions. Equation (4.3) is called the Heisenberg model. The charge distribution of a system of two spins connected on the behaviour of the spins if they are parallel or antiparallel, for the Pauli Exclusion Principle consists that two electrons of the same spin cannot be in the same place at the same time (zero probability of finding the two electrons at the same position). The two electrons are antiparallel. Therefore, the electrostatic energy and the relative orientation of the spins depend on each other: the exchange energy is defined by the difference in energy.

4.4 Analytical model of Antiferromagnetic resonance

4.4.1 Easy axis lying along x (β_1 > 0), magnetization m₁ (+x) and m₂ (-x)

no spin-hall current

We calculate the dispersion relation in the absence of spin-Hall current. For this case, it is reasonable to linearize the equations of motion due to the very small precession angle.

We include the uniaxial anisotropy field contribution to the torque, $\mathbf{h_{ani-1}} = \beta_1 (\mathbf{m_1} \cdot \mathbf{e}_x) \mathbf{e}_x$ and $\mathbf{h_{ani-2}} = \beta_1 (\mathbf{m_2} \cdot \mathbf{e}_x) \mathbf{e}_x$ proportional to β_1. The anisotropy field is decomposed into a static part $\mathbf{h}_{ani-1}^0 = \beta_1 (\mathbf{m_1^0} \cdot \mathbf{e}_x) \mathbf{e}_x$ for sub-lattice 1 and $\mathbf{h}_{ani-2}^0 = \beta_1 (\mathbf{m_2^0} \cdot \mathbf{e}_x) \mathbf{e}_x$ for sublattice 2 and a dynamic part $\beta_1 (\delta\mathbf{m_1} \cdot \mathbf{e}_z) \mathbf{e}_z$ for sub-lattice 1 and $\beta_1 (\delta\mathbf{m_2} \cdot \mathbf{e}_z) \mathbf{e}_z$ for sub-lattice 2.

In this case, with magnetizations along the easy axis (x axis), the active dynamic torques appearing in the linearized equations and associated to the uniaxial anisotropy field are $\delta\mathbf{m_1} \times \beta_1 (\mathbf{m_1^0} \cdot \mathbf{e}_x) \mathbf{e}_x$ for sublattice 1 and $\delta\mathbf{m_2} \times \beta_1 (\mathbf{m_2^0} \cdot \mathbf{e}_x) \mathbf{e}_x$ for sublattice 2.

Taking into account only first-order terms of the torques, the linearized Landau-Lifshitz takes the form:

$$
\begin{aligned}
i\omega\delta\mathbf{m_1} &= -\mathbf{m_1^0} \times \left[\lambda_{FM}\nabla^2\delta\mathbf{m_1} - \lambda_{AFM}\nabla^2\delta\mathbf{m_2} - \sigma\,\delta\mathbf{m_2} \right] + \delta\mathbf{m_1} \times \left[\sigma\mathbf{m_2^0} + \beta_1 (\mathbf{m_1^0} \cdot \mathbf{e}_x) \mathbf{e}_x \right] \\
i\omega\delta\mathbf{m_2} &= -\mathbf{m_2^0} \times \left[\lambda_{FM}\nabla^2\delta\mathbf{m_2} - \lambda_{AFM}\nabla^2\delta\mathbf{m_1} - \sigma\,\delta\mathbf{m_1} \right] + \delta\mathbf{m_2} \times \left[\sigma\mathbf{m_1^0} + \beta_1 (\mathbf{m_2^0} \cdot \mathbf{e}_x) \mathbf{e}_x \right]
\end{aligned}
\tag{4.4}
$$

Performing the Laplacian, it is possible to rewrite the equations of motion in the form:

$$
\begin{aligned}
i\omega\delta\mathbf{m_1} &= -\mathbf{m_1^0} \times \left[-\lambda_{FM}k^2\delta\mathbf{m_1} + \lambda_{AFM}k^2\delta\mathbf{m_2} + \sigma\,\delta\mathbf{m_2} \right] - \delta\mathbf{m_1} \times \left[\sigma\mathbf{m_2^0} + \beta_1 (\mathbf{m_1^0} \cdot \mathbf{e}_x) \mathbf{e}_x \right] \\
i\omega\delta\mathbf{m_2} &= -\mathbf{m_2^0} \times \left[-\lambda_{FM}k^2\delta\mathbf{m_2} + \lambda_{AFM}k^2\delta\mathbf{m_1} + \sigma\,\delta\mathbf{m_1} \right] - \delta\mathbf{m_2} \times \left[\sigma\mathbf{m_1^0} + \beta_1 (\mathbf{m_2^0} \cdot \mathbf{e}_x) \mathbf{e}_x \right]
\end{aligned}
\tag{4.5}
$$

The linearized LL equations in terms of components are:

$$
\begin{cases}
i\omega\delta m_1^y = -k^2 m_1^0 \lambda_{FM}\delta m_1^z + k^2 m_1^0 \lambda_{AFM}\delta m_2^z - \sigma m_1^0 \delta m_2^z + \sigma m_2^0 \delta m_1^z - \beta_1 m_1^0 \delta m_1^z \\
i\omega\delta m_1^z = k^2 m_1^0 \lambda_{FM}\delta m_1^y - k^2 m_1^0 \lambda_{AFM}\delta m_2^y + \sigma m_1^0 \delta m_2^y - \sigma m_2^0 \delta m_1^y + \beta_1 m_1^0 \delta m_1^y
\end{cases}
\tag{4.6}
$$

for sublattice 1 and:

$$\begin{cases} i\omega\,\delta m_2^y = -k^2 m_2^0 \lambda_{FM}\,\delta m_2^z + k^2 m_2^0 \lambda_{AFM}\,\delta m_1^z - \sigma m_2^0\,\delta m_1^z + \sigma m_1^0\,\delta m_2^z - \beta_1 m_2^0\,\delta m_2^z \\ i\omega\,\delta m_2^z = k^2 m_2^0 \lambda_{FM}\,\delta m_2^y - k^2 m_2^0 \lambda_{AFM}\,\delta m_1^y + \sigma m_2^0\,\delta m_1^y - \sigma m_1^0\,\delta m_2^y + \beta_1 m_2^0\,\delta m_2^y \end{cases} \quad (4.7)$$

for sublattice 2.

Rearranging the terms and merging the four equations, we get:

$$\begin{cases} -i\omega\,\delta m_1^y + \left(-k^2\lambda_{FM}m_1^0 + \sigma m_2^0 - \beta_1 m_1^0\right)\delta m_1^z + 0\,\delta m_2^y + \left(k^2\lambda_{AFM}m_1^0 - \sigma m_1^0\right)\delta m_2^z \\ \left(k^2\lambda_{FM}m_1^0 - \sigma m_2^0 + \beta_1 m_1^0\right)\delta m_1^y - i\omega\,\delta m_1^z + \left(-k^2\lambda_{AFM}m_1^0 + \sigma m_1^0\right)\delta m_2^y + 0\,\delta m_2^z \\ 0\,\delta m_1^y + \left(k^2\lambda_{AFM}m_2^0 - \sigma m_2^0\right)\delta m_1^z - i\omega\,\delta m_2^y + \left(-k^2\lambda_{FM}m_2^0 + \sigma m_1^0 - \beta_1 m_2^0\right)\delta m_2^z \\ \left(-k^2\lambda_{AFM}m_2^0 + \sigma m_2^0\right)\delta m_1^y + 0\,\delta m_1^z + \left(k^2\lambda_{FM}m_2^0 - \sigma m_1^0 + \beta_1 m_2^0\right)\delta m_2^y - i\omega\,\delta m_2^z \end{cases} \quad (4.8)$$

Note that, in the units chosen, all terms are dimensionless. In particular, $m_1^0 = 1$ and $m_2^0 = -m_1^0 = -1$

To determine the frequency dispersion we solve the determinant of the coefficients and we impose it equal to zero:

$$\det\begin{vmatrix} -i\omega & -k^2\lambda_{FM} - \sigma - \beta_1 & 0 & k^2\lambda_{AFM} - \sigma \\ k^2\lambda_{FM} + \sigma + \beta_1 & -i\omega & -k^2\lambda_{AFM} + \sigma & 0 \\ 0 & -k^2\lambda_{AFM} + \sigma & -i\omega & k^2\lambda_{FM} + \sigma + \beta_1 \\ k^2\lambda_{AFM} - \sigma & 0 & -k^2\lambda_{FM} - \sigma - \beta_1 & -i\omega \end{vmatrix} = 0 \quad (4.9)$$

By means of the substitution $\omega \to \gamma_0 M_0 \omega$ solutions are:

$$\omega_{1,2} = \pm\gamma_0 M_0\sqrt{\left[\beta_1 + 2\sigma + \left(\lambda_{FM} - \lambda_{AFM}\right)k^2\right]\left[\beta_1 + \left(\lambda_{FM} + \lambda_{AFM}\right)k^2\right]} \quad (4.10)$$

and $\omega_{3,4} = \omega_{1,2}$.

For the parameters used, $\beta_1 + \left(\lambda_{FM} - \lambda_{AFM}\right)k^2 \ll \sigma$. Hence:

$$\omega_{AFM} = \pm\gamma_0 M_0\sqrt{2\sigma\left[\beta_1 + \left(\lambda_{FM} + \lambda_{AFM}\right)k^2\right]} \quad \text{AFM ACOUSTIC MODE} \quad (4.11)$$

The terms inside the square root are dimensionless.

We get two couples of coincident solutions corresponding to the AFM ACOUSTIC MODE. The AFM resonance ($k \to 0$) is $\omega_0 = \pm\gamma_0 M_0 \sqrt{2\sigma\,\beta_1}$ (solution coincident with the one of [112]).

By introducing the explicit expressions of σ, β_1, λ_{FM} and λ_{AFM}, we get:

$$\omega_{AFM} = \pm\frac{4\gamma_0}{aM_0}\sqrt{A\left(K_U + 3Ak^2\right)} \tag{4.12}$$

The AFM resonance ($k \to 0$) is

$$\omega_{AFMR} = \pm\frac{4\gamma_0}{aM_0}\sqrt{A\,K_U} \tag{4.13}$$

It is possible to obtain the same result by using the complex magnetization representation. In this way, we reduce the number of equations of motion from four to two. We recall the four linearized equations:

$$\begin{cases} \dfrac{\partial\delta m_1^y}{\partial\tau} = +\left(-k^2\lambda_{FM}m_1^0 + \sigma m_2^0 - \beta_1 m_1^0\right)\delta m_1^z + \left(k^2\lambda_{AFM}m_1^0 - \sigma m_1^0\right)\delta m_2^z \\[2mm] \dfrac{\partial\delta m_1^z}{\partial\tau} = \left(k^2\lambda_{FM}m_1^0 - \sigma m_2^0 + \beta_1 m_1^0\right)\delta m_1^y + \left(-k^2\lambda_{AFM}m_1^0 + \sigma m_1^0\right)\delta m_2^y \\[2mm] \dfrac{\partial\delta m_2^y}{\partial\tau} = \left(k^2\lambda_{AFM}m_2^0 - \sigma m_2^0\right)\delta m_1^z + \left(-k^2\lambda_{FM}m_2^0 + \sigma m_1^0 - \beta_1 m_2^0\right)\delta m_2^z \\[2mm] \dfrac{\partial\delta m_2^z}{\partial\tau} = \left(-k^2\lambda_{AFM}m_2^0 + \sigma m_2^0\right)\delta m_1^y + \left(k^2\lambda_{FM}m_2^0 - \sigma m_1^0 + \beta_1 m_2^0\right)\delta m_2^y \end{cases} \tag{4.14}$$

By using the complex magnetization representation, we write $\delta m_1^+ = \delta m_1^y + i\,\delta m_1^z$ and $\delta m_2^+ = \delta m_2^y + i\,\delta m_2^z$. Rewriting the LL linearized equations in terms of these new variables on the first members, we get two equations:

$$\begin{cases} \dfrac{\partial \delta m_1^+}{\partial \tau} = \\ \left(-k^2\lambda_{FM}m_1^0 + \sigma m_2^0 - \beta_1 m_1^0\right)\delta m_1^z + \left(k^2\lambda_{AFM}m_1^0 - \sigma m_1^0\right)\delta m_2^z + \\ i\left[\left(k^2\lambda_{FM}m_1^0 - \sigma m_2^0 + \beta_1 m_1^0\right)\delta m_1^y + \left(-k^2\lambda_{AFM}m_1^0 + \sigma m_1^0\right)\delta m_2^y\right] \\ \dfrac{\partial \delta m_2^+}{\partial \tau} = \\ \left(k^2\lambda_{AFM}m_2^0 - \sigma m_2^0\right)\delta m_1^z + \left(-k^2\lambda_{FM}m_2^0 + \sigma m_1^0 - \beta_1 m_2^0\right)\delta m_2^z + \\ i\left[\left(-k^2\lambda_{AFM}m_2^0 + \sigma m_2^0\right)\delta m_1^y + \left(k^2\lambda_{FM}m_2^0 - \sigma m_1^0 + \beta_1 m_2^0\right)\delta m_2^y\right] \end{cases}$$

(4.15)

We multiply by –i both equations:

$$\begin{cases} -i\dfrac{\partial \delta m_1^+}{\partial \tau} = \\ i\left(k^2\lambda_{FM}m_1^0 - \sigma m_2^0 + \beta_1 m_1^0\right)\delta m_1^z + i\left(-k^2\lambda_{AFM}m_1^0 + \sigma m_1^0\right)\delta m_2^z + \\ \left[\left(k^2\lambda_{FM}m_1^0 - \sigma m_2^0 + \beta_1 m_1^0\right)\delta m_1^y + \left(-k^2\lambda_{AFM}m_1^0 + \sigma m_1^0\right)\delta m_2^y\right] \\ -i\dfrac{\partial \delta m_2^+}{\partial \tau} = \\ +i\left(-k^2\lambda_{AFM}m_2^0 + \sigma m_2^0\right)\delta m_1^z + i\left(k^2\lambda_{FM}m_2^0 - \sigma m_1^0 + \beta_1 m_2^0\right)\delta m_2^z + \\ \left[\left(-k^2\lambda_{AFM}m_2^0 + \sigma m_2^0\right)\delta m_1^y + \left(k^2\lambda_{FM}m_2^0 - \sigma m_1^0 + \beta_1 m_2^0\right)\delta m_2^y\right] \end{cases}$$

(4.16)

Expressing also the second members in terms of the new variables, we get:

$$\begin{cases} -\omega\,\delta m_1^+ = \left(k^2\lambda_{FM}m_1^0 - \sigma m_2^0 + \beta_1 m_1^0\right)\delta m_1^+ + \left(-k^2\lambda_{AFM}m_1^0 + \sigma m_1^0\right)\delta m_2^+ \\ -\omega\,\delta m_2^+ = \left(-k^2\lambda_{AFM}m_2^0 + \sigma m_2^0\right)\delta m_1^+ + \left(k^2\lambda_{FM}m_2^0 - \sigma m_1^0 + \beta_1 m_2^0\right)\delta m_2^+ \end{cases}$$

(4.17)

We write the determinant of the coefficients imposing that it is zero:

$$\det\begin{vmatrix} k^2\lambda_{FM} + \sigma + \beta_1 + \omega & -k^2\lambda_{AFM} + \sigma \\ k^2\lambda_{AFM} - \sigma & -k^2\lambda_{FM} - \sigma - \beta_1 + \omega \end{vmatrix} = 0$$

(4.18)

By means of the substitution $\omega \rightarrow \gamma_0 M_0 \omega$ again solutions are:

$$\omega_{AFM} = \pm\gamma_0 M_0 \sqrt{2\sigma\left[\beta_1 + \left(\lambda_{FM} + \lambda_{AFM}\right)k^2\right]} \quad \text{AFM ACOUSTIC MODE (4.19)}$$

being verified the condition $\beta_1 + \left(\lambda_{FM} - \lambda_{AFM}\right)k^2 \ll \sigma$. It is worthy to know that the optical mode exists when we have hard axis along z and easy xy plane, in the presence of current only.

4.5 THz oscillators based on antiferromagnets

Terahertz (THz) is generally utilized to submillimeter-wave energy that fills the frequency range from 300GHz to 3THz (1000–100 µm) (see figure 4.2) [113][114]. They have found widespread regions in electromagnetic spectrum. An excellent overview of THz can be found in quite various fields such as astronomy [115][116], medical imaging [117], material science [118], security screening [119], non-destructive testing [120], and communication [121][122].

With a proof of approach of AFMs memories [123][124][125][126] driven by spin-Hall effect in which play an obviously important role for the characteristics of magnetic behavior of the material (The origin of this strong magnetism is the presence of a spontaneous magnetization which is obtained by an antiparallel alignment of spins).
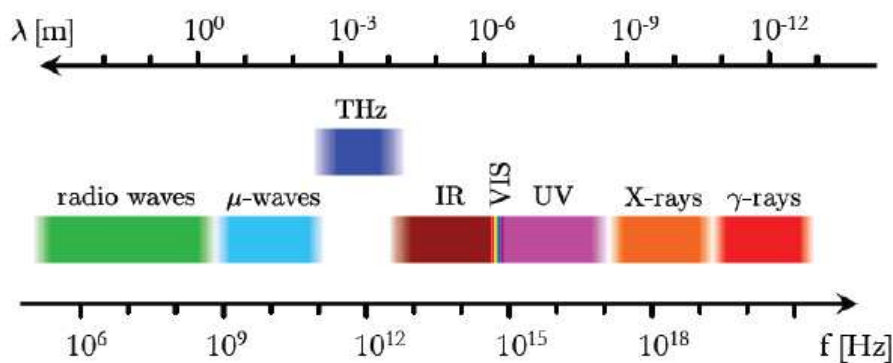
Fig. 4.2: Terahertz region is between infrared and microwave domains.

Despite great scientific interest, the AFM-based oscillators (ASHO) has not an experimental proof, and all the theoretical analysis of spins can be grouped into two sub-lattices with the magnetizations of the magnetic ions are antiferromagnetically coupled [129] and to figure out the dynamics we need to the Landau-Lifshitz-Gilbert-Slonczewski (LLGS) equations [130] and the macrospin approximation [128][129][130]. In addition, in the last papers the operational temperature of the oscillator was assumed to be much lower than the Néel temperature of the AFM thin films.

An important work has done by Puliafito and al [131] to understand the THz AFM dynamics driven by a damping-like torque originating from the spin Hall Effect. They performed a systematic study of the threshold currents and the output frequency as a function of different parameters such as spin-polarization direction, exchange constant, Gilbert damping, AFM thickness and Dzyaloshinskii–Moriya interaction (DMI) [131].

In this work, we use time-domain THz spectroscopy (TDS) to probe excitations in AFMs of two sub-lattices in the frequency range 0.1-0.6 THz.

The main motivation of this work is to investigate the characterisation of Antiferromagnets, in particular, on the calculation of their resonance frequency. Based on [131], Puliafito et al studied the threshold current as a function of the constant A, which corresponded to both non homogenous intrasublattice (typical for FM) and homogeneous intersublattice (necessary in AFM). In that study those two constant were considered equal each other. However, since in the overall coefficient of the homogeneous intersublattice there is the lattice constant a.

i) We studied the AFM resonance (not the critical threshold current) as a function of a, namely as a function of the homogeneous intersublattice exchange.

ii) We performed ferromagnetic resonance studies, where we fixed the amplitude of a sinusoidal current and change its frequency. We found that the ferromagnetic resonance frequency coincides with the frequency of the self-oscillation at the critical current.

4.5.1. Micromagnetic Model

The device consists of an AFM antiferromagnetic layer which is coupled to a heavy metal layer [130] , where the electric current flows by needs of the two coupled of contacts (AA' and BB'), (see Fig. 4.3(a-b). In our case we apply the current along the x direction AA' and the spin hall polarization is P along y (we take advantage of SHE). The AFM has a square cross section with dimensions 40x40 nm^2, whereas the thickness d varies from 1 to 5 nm. We model the AFM with two different sublattices and the average magnetization, of the spins that point parallel or antiparallel, of this two different sublattices are $\mathbf{m_1}$ and $\mathbf{m_2}$ (Fig. 4.3(c)). The two coupled Landau-Lifshitz-Gilbert equations plays an obviously role in determine the AFM dynamics of $\mathbf{m}1$ and $\mathbf{m}2$, and the SHE-driven spin-transfer torque has been considered by means of an additional Slonczewski-like torque term [126]:

$$\begin{cases} \dfrac{d\mathbf{m_1}}{d\tau} = -\left(\mathbf{m_1} \times \mathbf{h_{eff\text{-}1}}\right) + \alpha\mathbf{m_1} \times \dfrac{d\mathbf{m_1}}{d\tau} + d_J(\mathbf{m_1} \times \mathbf{m_1} \times \mathbf{p}) \\[4mm] \dfrac{d\mathbf{m_2}}{d\tau} = -\left(\mathbf{m_2} \times \mathbf{h_{eff\text{-}2}}\right) + \alpha\mathbf{m_2} \times \dfrac{d\mathbf{m_2}}{d\tau} + d_J(\mathbf{m_2} \times \mathbf{m_2} \times \mathbf{p}) \end{cases} \qquad (4.20)$$
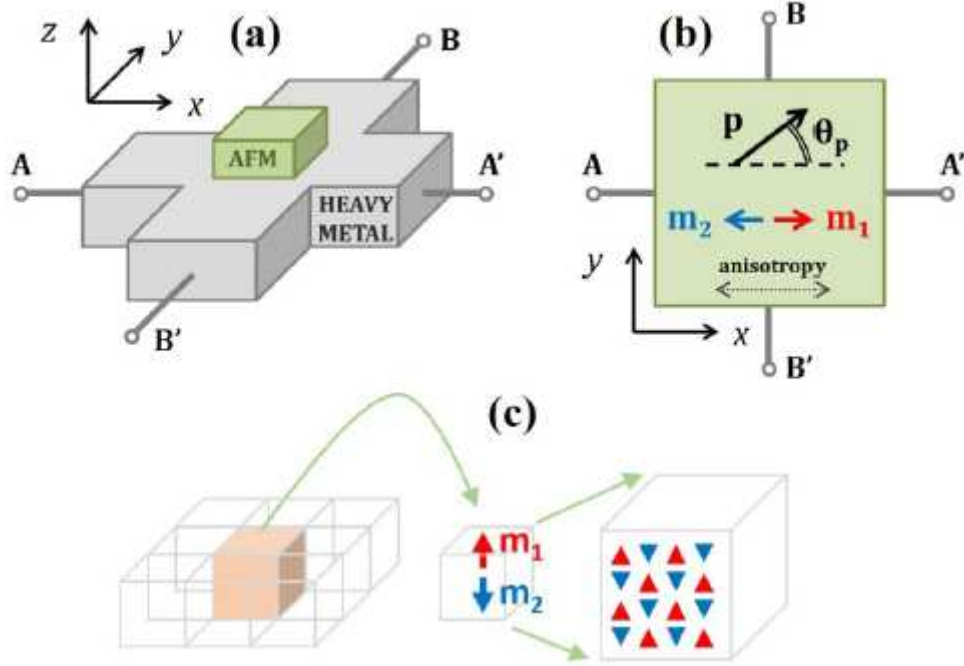
Fig. 4.3: Schemes of the device under investigation with the indication of the Cartesian reference systems. (a) A schematic of the bi-layered ASHO. The four terminals can be used for the application of charge currents, and for the measurement of the spin-Hall resistance. (b) Top view of the antiferromagnet, 1 **m** and 2**m** represent the initial configuration of the magnetizations of the two sub-lattices while **p** is the spin polarization. (c) Sketch of the idea at the basis of the continuous modeling of antiferromagnetic sub-lattices, for a given computational cell we consider that the average magnetization is given by the two vectors $\mathbf{m_1}$ and $\mathbf{m_2}$.

In the first part of Eqs. (4.20), $\mathbf{m_1}$ and $\mathbf{m_2}$ are therefore the magnetizations of the two sublattices, normalized with respect to the saturation magnetization M_S, and τ is the dimensionless time $\tau = \gamma_0 M_S t$, where γ_0 is the gyromagnetic ratio. In the second part, $\mathbf{h}_{\text{eff-1}}$ and $\mathbf{h}_{\text{eff-2}}$ are the normalized effective fields acting on the two sub-lattices, and α is the Gilbert damping. The third term represents the SHE-driven torque, where g is the Landè factor, B is the Bohr magneton, e is the electron charge, θ_{SH} is the spin-Hall angle, which represents the amount of charge current J converted into spin current J_S, $\theta_{SH} = J_S / J$. The vector **p** is the direction of the spin-Hall polarization, given by $\mathbf{p} = \hat{\mathbf{z}} \times \mathbf{j}$, where $\hat{\mathbf{z}}$ and $\mathbf{j}$ are the directions of the spin and electric currents. Indeed, **p** can be fixed in the *x-y* plane with an angle θ_P between 0° and 90°: if the electric current is applied only at the terminals B-B' (A-A'), then $\theta_P = 0^{\circ}$ ($\theta_P = 90^{\circ}$) resulting in a polarization collinear (normal) to the easy axis, see Fig. 4.3(b).

The effective fields constitute of the standard contributions from exchange, anisotropy, and demagnetizing:

$$\left\{ \begin{array}{l} \mathbf{h_{eff\text{-}1}} = \mathbf{h}_{exch\text{-}1} + \mathbf{h}_{ani\text{-}1} + \mathbf{h}_{demag\text{-}1} \\ \\ \mathbf{h_{eff\text{-}2}} = \mathbf{h}_{exch\text{-}2} + \mathbf{h}_{ani\text{-}2} + \mathbf{h}_{demag\text{-}2} \end{array} \right. \tag{4.21}$$

The exchange fields take into account both ferromagnetic coupling between neighbours in each sub-lattice and the antiferromagnetic coupling between the two sub-lattices.

This term is considered of atomistic origin in the reason of the two magnetization vectors $\mathbf{m_1}$ and $\mathbf{m_2}$ are at the same point and it is designed considering only the homogenous part,

$$\left\{ \begin{array}{l} \mathbf{h}_{exch\text{-}1} = \alpha_{exch-FM}\nabla^2\mathbf{m}_1 + \lambda_{AFM}\mathbf{m}_2 \\ \\ \mathbf{h}_{exch\text{-}2} = \alpha_{exch-FM}\nabla^2\mathbf{m}_2 + \lambda_{AFM}\mathbf{m}_1 \end{array} \right. \tag{4.22}$$

where $\alpha_{exch-FM} = 2A_{FM}/\mu_0 M_S^2$ and $\lambda_{exch-FM} = 4A_{AFM}/\mu_0 a^2 M_S^2$ contemplate the two main contributions, A_{FM} and A_{AFM} are the ferromagnetic and antiferromagnetic exchange constant, respectively, a is the lattice constant, and μ_0 is the vacuum permeability.

We take into consideration that the anisotropy fields originating from uniaxial material:

$$\left\{ \begin{array}{l} \mathbf{h}_{ani\text{-}1} = \alpha_{ani}\mathbf{m_1}.\mathbf{u}_k \\ \\ \mathbf{h}_{ani\text{-}2} = \alpha_{ani}\mathbf{m_2}.\mathbf{u}_k \end{array} \right. \tag{4.23}$$

where $\alpha_{ani} = 2K_U/\mu_0 M_S^2$, K_U is the uniaxial anisotropy constant, and $\mathbf{u}_k$ is the direction of the easy axis that is the x axis in our survey.

The demagnetizing field is investigated by solving the magnetostatic problem [97] for the total magnetization $(\mathbf{m_1} + \mathbf{m_2})/2$. As we interested in the dynamics of ultra-thin AFM films, we assume here substantially low value of the homogeneous exchange $A_{AFM}/a^2 = 1.25MJ/m^3$, being $a = 0.5$, 1 and 2 nm. The discretization cell used for the simulations is 2nm x2nm x d. When not specified, we have used the following parameters for the ASHO: $d = 5\,nm$, $M_S = 350\times10^3$ A/m, $\alpha = 0.05$, $K_U = 10^5$ J/m^3, $\theta_{SH} = 0.2$ and $A_{FM} = 0.5\times10^{-11}$ J/m.

4.5.2. RESULTS

4.5.2.1 Antiferromagnetic resonance vs a

In the case of easy axis, homogeneous intersublattice exchange constant A_{AFM} = 5.0 pJ/m, we consider three value of the atomic lattice constant a = 0.5nm, 1.0nm and 2.0nm corresponding to A_{AFM}/a^2 = 20MJ/m^3 (high intersublattice exchange), 5MJ/m^3, 1.25MJ/m^3 (low intersublattice exchange), respectively.

The AFMR decreases with the increase of a (see Fig.4.4) (i.e. AFMR increases with the increase of intersublattice exchange). Theoretical model confirms this result.
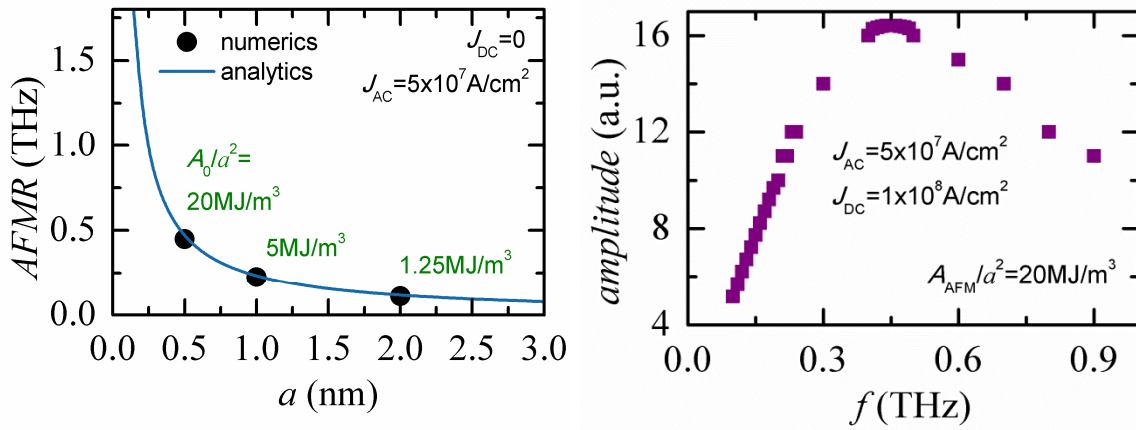
Fig. 4.4: (left figure) the antiferromagnetic resonance (AFMR) has been determined as a function of the atomic lattice constant a. (right figure) the amplitude as a function of the frequency (THZ).

4.5.2.2 AFMR vs A_{AFM-NH}

We consider three values of non-homogenous intersublattice exchange constant A_{AFM-NH} = 0.0 or 0.25 or 0.50 pJ/m and keep the same value of homogeneous intersublattice exchange constant (A_{AFM} = 5.0 pJ/m) for atomic lattice constant a = 0.5nm, which then corresponds to A_{AFM}/a^2 = 20MJ/m^3 (high intersublattice exchange) (see figure 4.5).
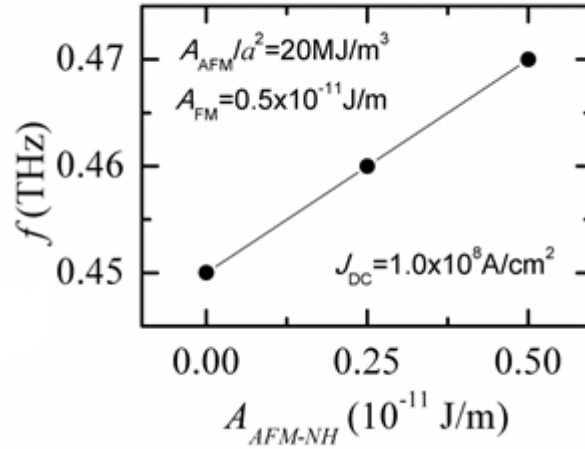
Fig. 4.5: the frequency as a function of the $A_{AFM\text{-}NH}$ which is a linear relation.

AFMR increases with the increase of the non-homogeneous intersublattice exchange.

4.5.2.3 AFMR vs DC current + dynamics

We have studied the case of non-homogenous intersublattice exchange constant $A_{AFM\text{-}NH}=0$ for atomic lattice constant $a = 0.5nm$ which is corresponding $A_{AFM}/a^2 = 20MJ/m^3$ (high intersublattice exchange) and the homogeneous intersublattice exchange constant $A_{AFM} = 5.0$ pJ/m. We obtain the results as shown in Figure 4.6.
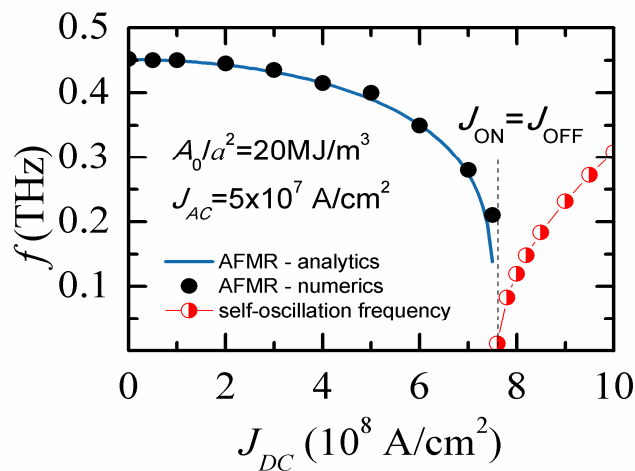
Fig. 4.6: AFMR decreases with the increase of the DC current. Dynamics are characterized by a precession of the two sublattices' magnetization around the spin-Hall polarization direction. The elimination current (J_{OFF}) coincides with the ignition current (J_{ON}) (right figure).

As the DC current increases, the AFMR decreases and, at the critical current, it corresponds to the frequency of the self-oscillation.

When $a = 2.0$nm, which corresponds to $A_{AFM}/a^2 = 1.25$MJ/m^3 (low intersublattice exchange), the switching off current (J_{OFF}) is lower than the ignition current (J_{ON}) (see fig.4.7). As the DC current increases, the AFMR decreases and, at the lower threshold current J_{OFF}, it goes close to the frequency of the self-oscillation.
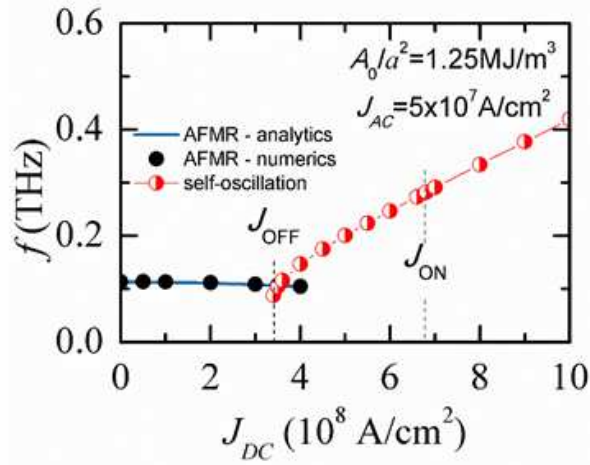
Fig. 4.7: AFMR still decreases with the increase of the DC current. Dynamics are still characterized by a precession of the two sublattices' magnetization around the spin-Hall polarization direction.

In the case of AFMR with easy plane, the A_{AFM} is about 5.0 pJ/m, the atomic lattice constant $a = 0.5$nm corresponding to $A_{AFM}/a^2 = 20$ MJ/m^3 (high intersublattice exchange) and A_{AFM-NH} is equal to zero (see Fig.4.8).
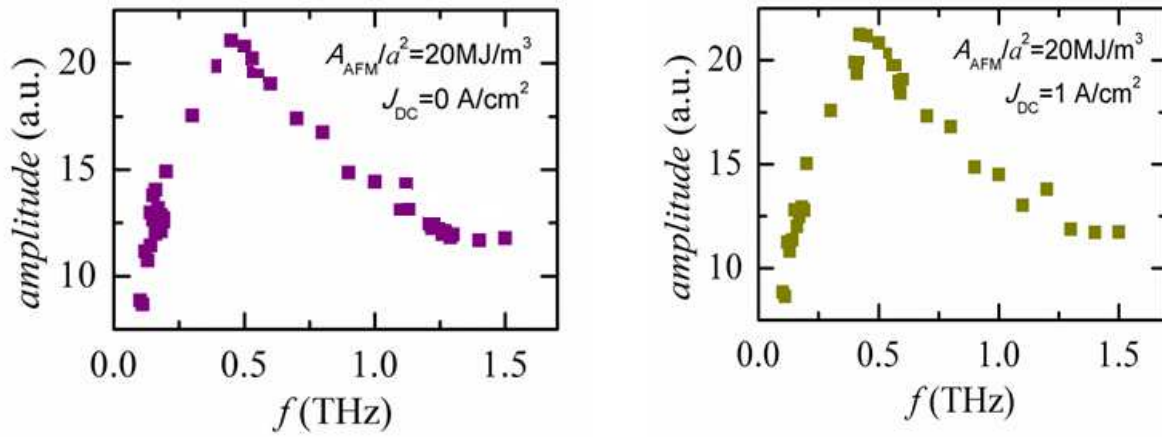
Fig. 4.8: AFMR characterised by a peak about 450 GHz

The resonance curves show clearly a peak about 450GHz.

5 Antiferromagnet MnO

This last chapter concerns an overview of nanoparticles and microparticles of manganese (II) oxide, their general structure and their magnetic properties. In section 5.1, an introduction to the properties of manganese oxides can be found. Section 5.2 deals with the experimental part including the synthesis and the characterization techniques used to analyse the samples. In section 5.3 the results obtained for MnO microparticles and discussion compared to MnO nanoparticles is presented and final conclusions.

5.1 Introduction

In the last few years, several studies have been devoted to nanoparticles due to their large interest for wide applications. It is well known that the sizes and morphology of nanomaterials have important effect on the properties and applications. For that reason, many investigations aim at logical control of shape, size and dimensionality of nanoparticles [132]. In particular, size of magnetic nanoparticles can influence some of their magnetic properties such as the Curie temperature, the spontaneous magnetization, and the anisotropic energy. One family of studied nanomaterials is the nanocrystalline oxides, which can be synthesized at the nanometric scale and possess fascinating magnetic and electronic properties due to the change in bands and their structure. Among them, we mention manganese (II) oxide (MnO) which is an important complex of metallic elements. Many studies were dedicated to this compound due to its interesting and various uses, like catalyst [133] [134], soft magnetic material [135], electrode for rechargeable lithium batteries [137] [138], ion exchanger, sensor, etc.

It is known that Manganese can form the stable oxides MnO, Mn_2O_3, Mn_3O_4, and MnO2 in addition to the metastable Mn_5O_8. These oxides could transform one into the other during the oxidation process. This transformation exists through various relations among the different manganese oxides. As an example, Manganese (II) oxide, MnO, known as mineral manganosite, oxidizes according to the following:

$$MnO \xrightarrow{\sim 390°C} Mn_3O_4 \xrightarrow{\sim 450°C} Mn_2O_3$$
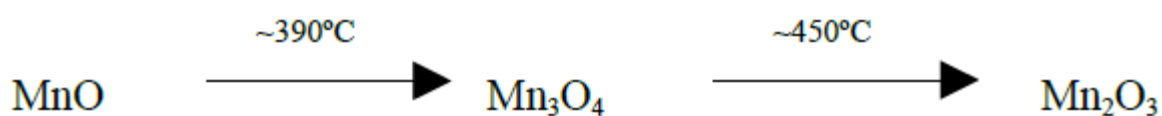
During transformation, and due to exposure to air, Bulk MnO assists a change of colours; the green crystalline solid becomes dark brown [138].

In our study, we focus on MnO, which is considered a model structure to study the theoretical properties of electronic and magnetic system of rock salt oxide [139] [140].
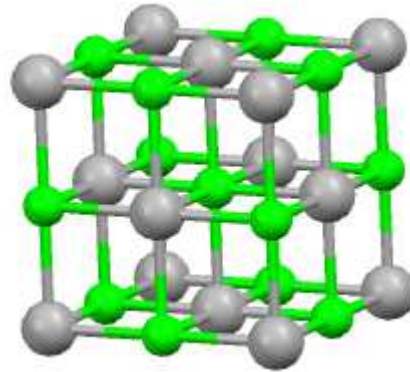
Fig. 5.1: MnO structure [141].

MnO nanoparticles show a ferromagnetic behaviour, whereas bulk MnO is antiferromagnetic with a transition temperature of ∼118K [139] [140].

The magnetic properties for manganese oxide range from AFM to Ferro- and ferrimagnetic properties with structures including the halite, as well as spinel. These properties are influenced strongly by finite size effect. Indeed, they depend on the crystal structure and the oxidation state. For more magnetic properties of MnO (see fig. 5.2) [142].

Néel temperature

T_N			
	118.5 K	heat capacity	81K
	117.9 K	magnetic susceptibility	81J
	116.9 K	Moessbauer data	67S
	116 K	magnetic susceptibility	61B
	117 K	magnetic susceptibility	65L
	117.8 K	heat capacity	51T
	117.7 K	neutron data	66L
	119.7 K	neutron data	74P
	117.5 K	critical neutron scattering	78B

Fig. 5.2: The magnetic properties for MnO

5.2 Experimental Part

5.2.1 Materials and synthesis

All of the reagents were used without further purification. For the synthesis of hierarchical MnO_2, manganese sulphate ($MnSO_4 \cdot H_2O$, 8 mmol) and ammonium persulfate ($NH_4S_2O_8$, 8 mmol) were firstly dissolved in 40 mL of deionized water by stirring, which was then transferred to a Teflon-lined stainless steel autoclave (50 mL). This autoclave was sealed and maintained at 90ºC for hours. Finally the resultant MnO_2 powder was collected by filtration, washed with distilled water and absolute ethanol for several times, and dried in air at 80 ºC. MnO was obtained by the calcinations of the as-prepared MnO_2 at 500 ºC in Ar/H_2 atmosphere (volume ratio 95:5).

5.2.2 Morphological Characterization

5.2.2.1 Scanning electron microscopy (SEM)

This technique has been used to study the morphology and particle size of the synthesized polycrystalline samples, as well as their degree of homogeneity (see figure 5.3).

For this study, a Zeiss Fesem Ultra Plus from the Research Infrastructure Network for Investigation and Technological Development, RIADIT, of the Universidade de Santiago de Compostela was used.

In all cases, the studies were performed on patterned samples.

Fig. 5.3: Photograph of Zeiss Fesem Ultra Plus microscope.

5.2.2.2 Transmission electron microscopy (TEM)

To carry out these studies, a transmission electron microscope JEOL, model JEM-1011, which has a tungsten filament and works at an acceleration potential of 100 kV have been used (see figure 5.4). This equipment belongs to the Microscopy Unit of the RIADIT of the Universidade de Santiago de Compostela.

For the study of the samples by TEM, a very small amount of them was ground and dispersed in propan-2ol, then deposited on a copper grid covered with a polyvinylformol film and shaded with a thin layer of carbon.

Fig. 5.4: Photograph of JEOL JEM-1011 microscope.

5.2.3. Structural Characterization

5.2.3.1. X ray powder diffraction (XRPD)

X-ray diffraction of crystalline powder (see figure 5.5) allowed us to study the formation of the crystalline phase during the different stages of synthesis, as well as the structural characteristics of the products obtained.

The equipment used was a PaNalytical-EMPYREAM automatic diffractometer with Kα radiation from Cu (λ = 1.5418 Å) and equipped with a graphite monochromator. This equipment belongs to the Structural Analysis Unit of the RIADIT of the Universidade de Santiago.

The measurement conditions were: 40 kV, 30 mA, angular range of measurement of $15° \leq 2\theta_B \leq 80°$, and two sweep speeds were used:

a) Fast sweep: 1º / minute (step = 0.050º, time = 3 s), used to follow the evolution of the phases after the different thermal treatments.

b) Slow sweep: 0.09º / minute (step = 0.015º, time = 10 s), used to achieve a more precise characterization of the phases by Rietveld refinement.

Fig. 5.5: Photograph of PaNalytical-EMPYREAM diffractometer.

5.2.3.2. Data processing

To carry out the adjustment of X-ray diffractograms using the Rietveld method, we used the Fullprof [143] program.

The profile form used was an asymmetric Pseudo-Voigt function, which is a linear combination of a Gaussian and a Lorentzian function.

5.2.4 Magnetic Properties

The magnetic properties were measured in the Superconducting Quantum Desing, SQUID (see figure 5.6 left), and vibrating sample magnetometers (see figure 5.6 right), VSM, model DMS-1660, belonging to the Magnetism and Nanotechnology group and the Laboratory of Low Temperatures and Superconductivity of the University of Santiago de Compostela.

These equipment allow to study the magnetic susceptibility of the samples according to the temperature, $\chi_m (T)$, and the magnetization depending on the applied field, M (H), at different temperatures.

Fig. 5.6: Photograph of SQUID (left) and VSM (right).

5.2.4.1. Magnetic susceptibility measurements as a function of temperature, χ_m (T)

The measurements were performed in the temperature range 5 $\leq$T (K) $\leq$ 300 and applying, in general, a magnetic field of 100 Oe.
Measurements were made under cooling conditions without field, ZFC, (Zero Field Cool) and under cooling conditions with field, FC, (Field Cool), collecting the data in intervals of 5 K.

5.2.4.2. Magnetic susceptibility measurements as a function of magnetic field, M(H)

For the realization of these measures the SQUID has been used. The samples were previously demagnetized by heating them to a temperature higher than 300 K and then cooled down to the measurement temperature, in our case 5 K, and in the absence of a magnetic field. A magnetic field was then applied whose value was varied according to the sequence:

$$50 \text{ kOe} \rightarrow 0 \text{ Oe} \rightarrow \text{-50 kOe} \rightarrow 0 \text{ Oe} \rightarrow 50 \text{ kOe}$$

The data were recorded at intervals of 1000 Oe, between 0 and 10000 Oe, while between 10000 and 50000 Oe were collected at intervals of 5000 Oe.

5.3 Results and Discussion

5.3.1 Structural characterization

The XRD pattern (figure 5.7) exhibits five characteristic peaks at $2\theta_B$ = 34.90, 40.64, 58.76, 70.21 and 73.77° that correspond to (111), (200), (220), (311), and (222) reflections (JCPDS no 07-0230), indicating the formation of well-ordered cubic MnO with space group Fm3m.
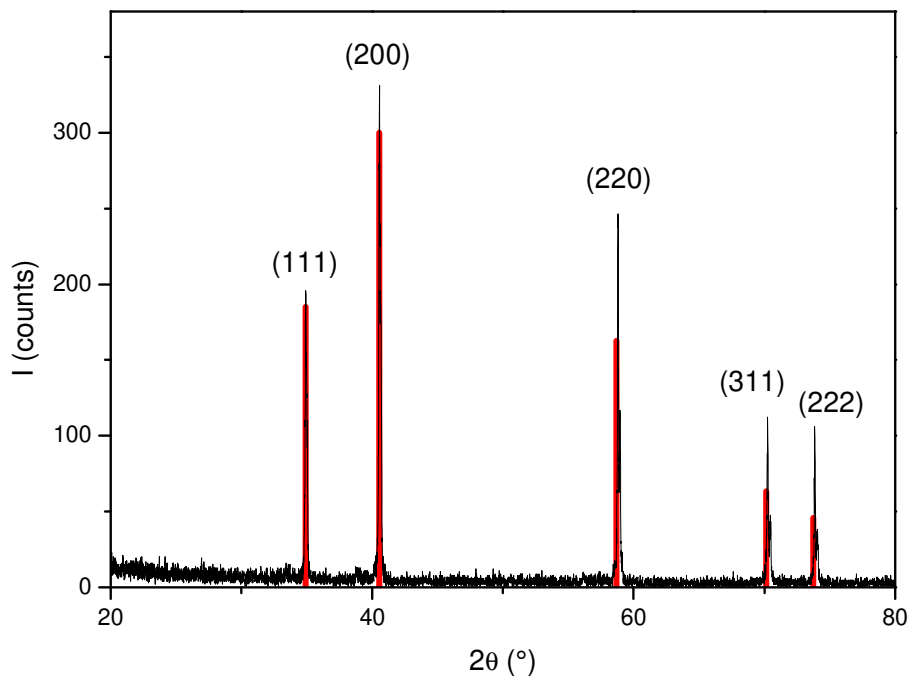
Fig. 5.7: X-ray powder diffraction (XRPD) of the MnO sample with the Miller index (hkl). The red line represents the MnO reference pattern (JCPDS no 07-0230).

The length of the cubic unit cell a is calculated using the following equation:

$$a = \frac{\lambda\sqrt{h^2 + k^2 + l^2}}{2\sin\theta_B}$$

Where λ_{Cu}= 1.5405 Å, (h,k,l) is the Miller index and θ_B is the Bragg angle.

$$a = 4.4388\ \overset{\circ}{A}$$

in comparison with the results obtained by Ghosh et al [144] we can find a similar results of MnO nanoparticle about 4.429 $\overset{\circ}{A}$.

5.3.2 Morphological characterization

Figure 5.8 shows SEM images of MnO. The morphology of the microparticles show a regular structure with triangular lamellae that stock in an ordered fashion.
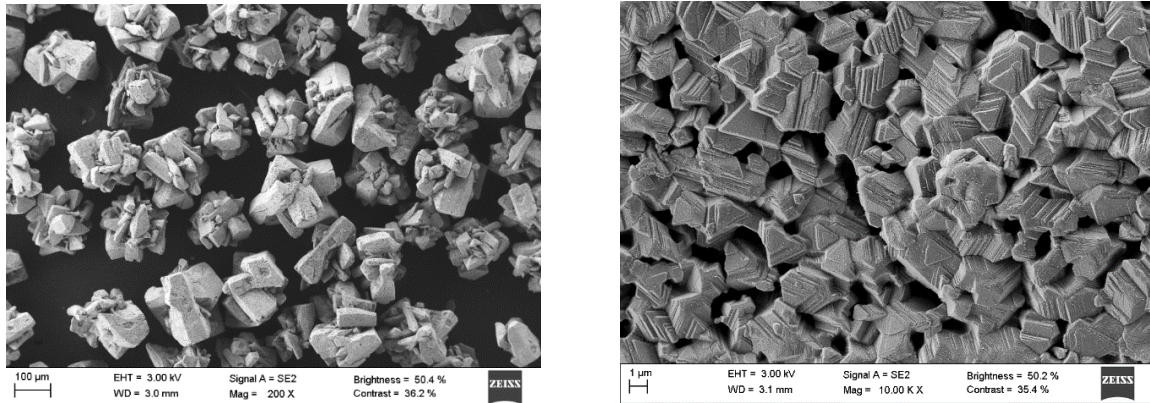
Fig. 5.8: Scanning electron microscopy images (SEM) for MnO microparticles (right) and holes (left).

We have calculated the size of MnO microparticles, by the ImageJ program, it is around 173 µm (see fig. 5.8) with an error ± 1.06.

5.3.3 Magnetic characterization

Figure 5.9 shows the magnetization data of one sample with average diameter of $0.6493 A^{o}$. The FC and ZFC data show divergence at low temperature. The magnetization in the FC data shows a marked increase at low temperature, where a shoulder like feature is also evident. The ZFC data clearly show maxima corresponding to the antiferromagnetic transition.
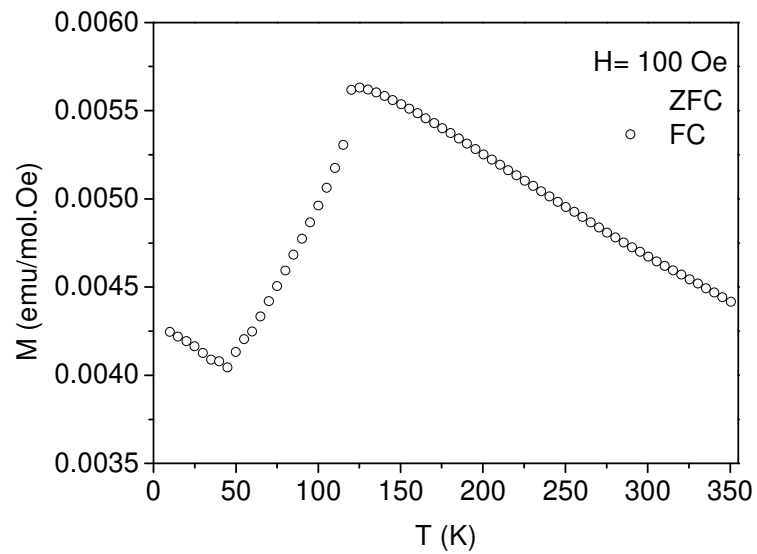
Fig. 5.9: Temperature dependence of magnetization of MnO particles under FC and ZFC conditions using a magnetic field of 100 kOe.

Figure 5.10 shows the inverse of the magnetic susceptibility as a function of temperature. In order to calculate the inverse of χ^{-1} we just take the linear part of the paramagnetic region.
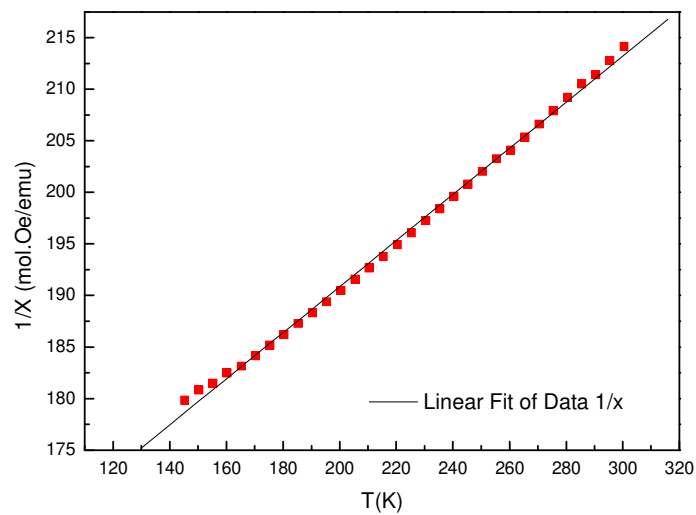
Fig. 5.10: The inverse of the magnetic susceptibly as a function of the temperature.

The Curie–Weiss law describes the magnetic susceptibility χ of a ferromagnet in the paramagnetic region above the Curie point:

$$\chi = \frac{C}{T - Tc}$$

$$\frac{1}{\chi} = \frac{T - T_c}{C} = \frac{T}{C} - \frac{Tc}{C}$$

$$y = ax + b$$

$$a = \frac{1}{C} \rightarrow C = \frac{1}{a} = \frac{1}{146.15861} = 0.00684$$

$$b = -\frac{Tc}{C} \rightarrow Tc = -b * C = -0.2235 * 0.00684 = -0.00153 K$$

where C is a material-specific Curie constant, T is absolute temperature and T_c is the Curie temperature, both measured in kelvin.

We can see that the Curie–Weiss temperature for microparticles is near zero, $T_c=0K$, *Noting that we have obtained this result by* Ghosh et al [144].

Fig. 5.11 shows the variation of the magnetization with field at 10 K for the MnO microparticles to reveal the occurrence of hysteresis at low temperatures, the H_C value being 201.21 Oe.
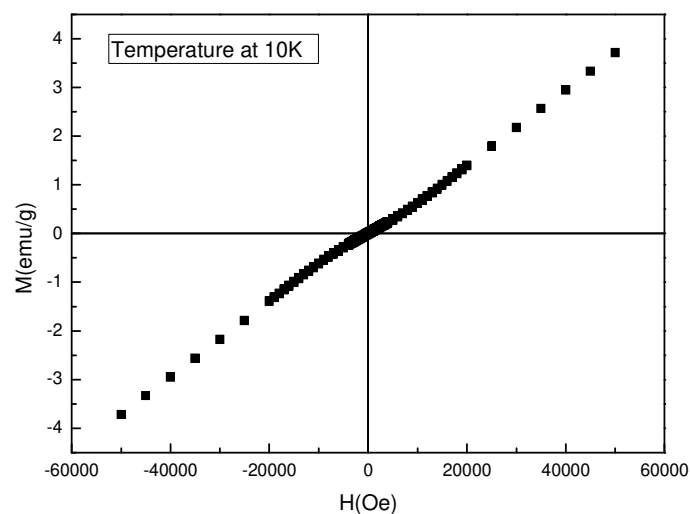
Fig. 5.11: Field dependence of the magnetization of the MnO microparticles measured at 10 K.

This results confirm the antiferromagnetic (AF) phase transition at the Néel temperature T_N of 118K, in the powder crystal form. Above this value MnO is paramagnetic phase. (See fig. 5.10). Good agreement between theory and experiment is obtained.

5.4 Conclusions

The main point of our experimental work is to study the magnetic properties of microparticles MnO. Magnetic properties of the well-characterised microparticles of these antiferromagnetic oxides reveal the presence of superparamagnetic, as evidenced the magnetic hysteresis at low temperature. Interestingly, the blocking temperature shows the phase separation between superparamagnetic and AFM phase around a value 118 K which is fairly represented by the high Néel temperatures. The results show a confirmation with the study of the nanoparticles.

6 Chapter 6
Journal Articles

5.1 Published articles

J1. Riccardo Tomasello, Anna Giordano, Stefano Chiappini, Roberto Zivieri, Giulio Siracusano, Vito Puliafito, <u>Israa Medlej</u>, Aurelio La Corte, Bruno Azzerboni, Mario Carpentieri, Zhongming Zeng, Giovanni Finocchio

"Micromagnetic understanding of the skyrmion Hall angle current dependence in perpendicularly magnetized ferromagnets".

5.2 Submitted articles

J2. <u>Israa Medlej</u>*, Abass Hamadeh, Fouad El Haj Hassan

"Skyrmion based random bit generator".

Accepted in Physica B.

BIBLIOGRAPHY

[1]   S.A.Wolf, J. Lu, M. R. Stan, Senior Member IEEE, E. Chen, Senior Member IEEE, and D. M.Trege, "The promise of nanomagnetics and spintronics for future logic and universal memory" *Proceedings of the IEEE,* **98**, 12 (2010).

[2]   M. N. Baibich, J. M. Broto, A. Fert, F. Nguyen Van Dau, F. Petroff, P. Etienne, G. Creuzet, A. Friederich, and J. Chazelas, "Giant magnetoresistance of (001) Fe/(001) Cr magnetic superlattices" *Physical review letters*, **61**, 21 (1988).

[3]   L.Berger, "A simple theory of spin-wave relaxation in ferromagnetic metals" *Journal of physics and chemistry of solids*, **38**, 1321-1326 (1977).

[4]   J.C. Slonczewski, "Current-driven excitation of magnetic multilayers" *Journal of Magnetism and Magnetic Materials*, **159**, 1-2 (1996).

[5]   L. Berger, "Emission of spin waves by a magnetic multilayer traversed by a current" Physical *Review B,* **54**, 13 (1996).

[6]   S.S.P. Parkin, M. Hayashi, and L. Thomas, "Magnetic domain-wall racetrack memory" *Science* **320**, 5873 (2008)

[7]   O. Boulle, J. Kimling, P. Warnicke, M. Kläui, U. Rüdiger, G. Malinowski, H. J. M. Swagten, B. Koopmans, C. Ulysse, and G. Faini, "Nonadiabatic spin transfer torque in high anisotropy magnetic nanowires with narrow domain walls" *Physical review* letters, **101**, 216601 (2008).

[8]   X.Z. Yu, N. Kanazawa, W.Z. Zhang, T. Nagai, T. Hara, K. Kimoto, Y. Matsui, Y. Onose, and Y. Tokura, "Skyrmion flow near room temperature in an ultralow current density" *Nature communications*, **3**, 988 (2012)

[9]   J. Sampaio, V Cros , S Rohart , A Thiaville, and A Fert . "Nucleation, stability and current-induced motion of isolated magnetic skyrmions in nanostructures" *Nature nanotechnology,* **8**, 11 (2013).

[10]   T. Kishi, H. Yoda, T. Kai, T. Nagase, E. Kitagawa, M. Yoshikawa, K. Nishiyama, T. Daibou, M. Nagamin. M. Amano, S. Takahashi, M. Nakayama, N. Shimomura, H. Aikawa, S. Ikegawa, S. Yuasa, K. Yakushiji, H. Kubota, A. Fukushima, M. Oogane, T. Miyazaki, and K. Ando "Lower-current and fast switching of a perpendicular TMR for high speed and high density spin-transfer-torque MRAM" *Electron Devices Meeting 2008 IEEE*, (2008).

[11]   T. Yang, T. Kimura, and Y. Otani , "Giant spin-accumulation signal and pure spin-current-induced reversible magnetization switching" *Nature Physics,* **4**, 11 (2008).

[12]   I. M. Miron, K. Garello, G. Gaudin, P.-J. Zermatten, M. V. Costache, S. Auffret, S. Bandiera, B. Rodmacq, A. Schuhl, and P. Gambardella, "Perpendicular switching of a single ferromagnetic layer induced by in-plane current injection" *Nature*, **476**, 189–193 (2011)

[13]   D. Houssameddine, U. Ebels, B. Delaët, B. Rodmacq, I. Firastrau, F. Ponthenier, M. Brunet, C. Thirion, J.-P. Michel, L. Prejbeanu-Buda, M.-C. Cyrille, O. Redon, and B. Dieny. "Spin-torque oscillator using a perpendicular polarizer and a planar free layer" *Nature materials* **6**, 447–453 (2007)

[14]   O. Boulle, V. Cros, J. Grollier, L. G. Pereira, C. Deranlot, F. Petroff, G. Faini and J. Barnaś, and A. Fert, "Shaped angular dependence of the spin-transfer torque and microwave generation without magnetic field" *Nature Physics*, **3**, 492–497 (2007).

[15]   V. E. Demidov, S. Urazhdin, H. Ulrichs, V. Tiberkevich, A. Slavin, D. Baither, G. Schmitz, and S. O. Demokritov, "Magnetic nano-oscillator driven by pure spin current" *Nat. Mater.,* **11**, 1028–1031 (2012).

[16]   D. C. Ralph, and M. D. Stiles, "Spin-Transfer Torques", *J. Magn. Magn. Mater*. **320**, 1190-1216 (2008).

[17]   G. Bertotti, "Hysteresis in Magnetism - For Physicists, Materials Scientists and Engineers", *Academic Press* (1998).

[18]   B. Hillebrands, and K. Ounadjela, "Spin Dynamics in Confined Magnetic Structures I",   *Springer*, Berlin (2002).

[19]   B. Hillebrands, and A. Thiaville, "Spin Dynamics in Confined Magnetic Structures III", *Springer*, Berlin (2006).

[20]   L. D. Landau, and E. Lifshitz, "On the theory of the dispersion of magnetic permeability in ferromagnetic bodies", *Phys. Z. Sowjetunion* **8**,153-169 (1935).

[21]   L. D. Landau, and E. Lifshitz, "Electrodynamics of Continuous Media", *Pergamon Press*, Oxford (1960).

[22]   W. F. Brown, "Magnetostatic Principles in Ferromagnetism", *North-Holland Pub. Co.* (1962).

[23]   W. F. Brown, "Micromagnetics", *Interscience Tracts on Physics and Astronomy*, Interscience Publishers (John Wiley and Sons), *New York – London* (1963).

[24]   W. F. Jr. Brown, and A. E. La Bonte, "Structure and energy of one-dimensional domain walls in ferromagnetic thin films", *J. Appl. Phys.* **36**, 1380–1386 (1965).

[25]   J. D- Jackson. "Classical Electrodynamics", *New York: Wiley* (1999).

[26]   T. Gilbert, "A Lagrangian formulation of the gyromagnetic equation of the magnetic field", *Phys. Z. Sowjetunion* **100,** 1243 (1955).

[27]   T. Gilbert, "A phenomenological theory of damping in ferromagnetic materials", *IEEE Trans. Magn.* **40**, 3443 (2004).

[28]   A. Landé, "Über den anomalen Zeemane_ekt (Teil I)", *Zeitschrift für Physik* **5,** 231 (1921).

[29]   A. Landé, "Über den anomalen Zeemane_ekt (Teil II)", *Zeitschrift für Physik* **7,** 398 (1921).

[30]   J. Slonczewski, "Currents, torques, and polarization factors in magnetic tunnel junctions", *Phys. Rev B*, **71**, 024411, (2005).

[31]   A. Slavin, and V. Tiberkevich, "Nonlinear Auto-Oscillator Theory of Microwave Generation by Spin-Polarized Current", *IEEE Trans. Magn.* **45**, 1875-1918 (2009).

[32]   S. Zhang, and Z. Li, "Roles of Nonequilibrium Conduction Electrons on the Magnetization Dynamics of Ferromagnets", *Phys. Rev. Lett.* **93**, 127204 (2004).

[33]   S. Zhang, and Z. Li, "Roles of Nonequilibrium Conduction Electrons on the Magnetization Dynamics of Ferromagnets", *Phys. Rev. Lett.* **93**, 127204 (2004).

[34]   W.-G. Wang, M. Li, S. Hageman, and C. L. Chien, "Electric-field-assisted switching in magnetic tunnel junctions", *Nat. Mater.* **11**, 64-68 (2012).

[35]   J. Zhu, J. A. Katine, G. E. Rowlands, Y.-J. Chen, Z. Duan, J. G. Alzate, P. Upadhyaya, J. Langer, P. K. Amiri, K. L. Wang, and I. N. Krivorotov, "Voltage-Induced Ferromagnetic Resonance in Magnetic Tunnel Junctions", *Phys. Rev. Lett.***108**, 197203 (2012).

[36]   S. Ikeda, K. Miura, H. Yamamoto, K. Mizunuma, H. D. Gan, M. Endo, S. Kanai, J. Hayakawa, F. Matsukura, and H. Ohno, "A perpendicular-anisotropy CoFeB–MgO magnetic tunnel junction", *Nat. Mater.* **9**, 721-724 (2010).

[37]   T. Maruyama, Y. Shiota, T. Nozaki, K. Ohta, N. Toda, M. Mizuguchi, A. A. Tulapurkar, T. Shinjo, M. Shiraishi, S. Mizukami, Y. Ando, and Y. Suzuki, "Large voltage-induced magnetic anisotropy change in a few atomic layers of iron", *Nat. Mater.* **4**, 158-161 (2008).

[38]   J. E. Hirsch, "Spin Hall effect", *Phys. Rev. Lett.* **83**, 1834 (1999).

[39]   L. Liu, C.-F. Pai, Y. Li, H. W. Tseng, D. C. Ralph, and R. A. Buhrman, "Spin-Torque Switching with the Giant Spin Hall Effect of Tantalum", *Science* **336**, 555-558 (2012).

[40]   V. E. Demidov, S. Urazhdin, H. Ulrichs, V. Tiberkevich, A. Slavin, D. Baither, G.Schmitz, and S. O. Demokritov, "Magnetic nano-oscillator driven by pure spin current", *Nat. Mater.* **11**, 1028-1031 (2012).

[41]   L. Liu, C.-F. Pai, D. C. Ralph, and R. A. Buhrman, "Current-induced switching of perpendicularly magnetized magnetic layers using spin torque from the Spin-Hall effect", *Phys. Rev. Lett.* **109**, 186602 (2012).

[42]   P. Gambardella, and I. M. Miron, "Current-induced spin–orbit torques", *Phil. Trans.R. Soc. A* **369**, 3175–3197 (2011).

[43]   A. Manchon, and S. Zhang, "Theory of spin torque due to spin-orbit coupling", *Phys. Rev. B* **79**, 094422 (2009).

[44]   H. Kontani, J. Goryo, and D.S. Hirashima, "Intrinsic Spin Hall Effect in s-wave Superconducting State: Analysis of Rashba Mode", *Physical Review Letters* **8**, 102-086602 (2009).

[45]   E.I. Rashba, "Spin–orbit coupling and spin transport", *Physica E* **34,** 31–35 (2006).

[46]   M. I.Dyakonov, and V. I. Perel, "Current-induced spin orientation of electrons in semiconductors", *Phys. Lett. A* **35**, 459 (1971).

[47]   S. Rohart, and A. Thiaville, "Skyrmion confinement in ultrathin film nanostructures in the presence of Dzyaloshinskii- Moriya interaction", *Phys. Rev. B* **88**, 184422 (2013).

[48]   T. H. R. Skyrme, "A unified field theory of mesons and baryons", *Nucl. Phys.* **31,** 556–569 (1962)

[49]   C. Moutafis, S. Komineas, and J. A. C. Bland, "Dynamics and switching processes for magnetic bubbles in nanoelements", *Phys. Rev. B* **79**, 224429 (2009).

[50]   G. Finocchio, V. Puliafito, S. Komineas, L. Torres, O. Ozatay, T. Hauet and B. Azzerboni, "Nanoscale spintronic oscillators based on the excitation of confined soliton modes", *J. Appl. Phys.* **114,** 163908 (2013).

[51]   H.-B. Braun, "Topological effects in nanomagnetism: from superparamagnetism to chiral quantum solitons", *Adv. Phys.* **61**, 1-116 (2012)

[52]   Y. Zhou and M. Ezawa, "A reversible conversion between a skyrmion and a domain-wall pair in a junction geometry", *Nat. Comm.* **5**, 4652 (2014).

[53]   T. Shinjo, T. Okuno, R. Hassdorf, K. Shigeto, and T. Ono, "Magnetic Vortex Core Observation in Circular Dots of Permalloy", *Science* **289**, 930-932 (2000).

[54]   A. Giordano, V. Puliafito, L. Torres, M. Carpentieri, B. Azzerboni, and G. Finocchio, "Micromagnetic study of Spin-Transfer-Driven vortex dipole and vortex quadrupole dynamics", *IEEE Trans. Magn.* **50**, 4300404 (2014).

[55]   A. Fert, V. Cros, and J. Sampaio, "Skyrmions on the track", *Nat. Nanotech.* **8**, 152-156 (2013).

[56]   N. Nagaosa, and Y. Tokura, ''Topological properties and dynamics of magnetic skyrmions,'' *Nat. Nanotechnol*., **8**, 899–911, (2013).

[57]   G. Finocchio, F. Büttner, R. Tomasello, M. Carpentieri, and M. Kläui ''Magnetic skyrmions: from fundamental to applications,'' *J. Phys. D. Appl. Phys*., **49**, 423001, (2016).

[58]   S. Muhlbauer, B. Binz, F. Jonietz, C. Pfleiderer, A. Rosch, A. Neubauer, R. Georgii, and P. Böni, ''Skyrmion Lattice in a Chiral Magnet,'' Science (80-.). **323**, 915–919, (2009).

[59]   A. Neubauer, C. Pfleiderer, B. Binz, A. Rosch, R. Ritz, P. G. Niklowitz, and P. Böni, ''Topological hall effect in the a phase of MnSi,'' *Phys. Rev. Lett.*, **102**, 186602, (2009).

[60]   X. Z. Yu, Y. Onose, N. Kanazawa, J. H. Park, J. H. Han, Y. Matsui, N. Nagaosa, and Y. Tokura,   ''Real-space observation of a two-dimensional skyrmion crystal,'' *Nature*, **465**, 901–4, (2010).

[61]   S. X. Huang, and C. L. Chien, ''Extended Skyrmion Phase in Epitaxial FeGe111 Thin Films,'' *Phys. Rev. Lett.*, **108**, 267201, (2012).

[62]   I. Dzyaloshinsky, ''A thermodynamic theory of 'weak' ferromagnetism of antiferromagnetics,'' *J. Phys. Chem. Solids*., **4**, 241–255, (1958).

[63]   T. Moriya, ''New Mechanism of Anisotropic Superexchange Interaction_Moriya,'' *Phys. Rev. Lett.*, **4**, 4–6, (1960).

[64]   R. Tomasello, E. Martinez, R. Zivieri, L. Torres, M. Carpentieri, and G. Finocchio, ''A strategy for the design of skyrmion racetrack memories,'' *Sci. Rep.*, **4**, 6784, (2014).

[65]   A. Giordano, R. Verba, R. Zivieri, A. Laudani, V. Puliafito, G. Gubbiotti, R. Tomasello, G. Siracusano, B. Azzerboni, M. Carpentieri, A. Slavin, and G. Finocchioet al., "Spin-Hall nano-oscillator with oblique magnetization and Dzyaloshinskii-Moriya interaction as generator of skyrmions and nonreciprocal spin-waves,'' *Sci. Rep.*, **6**, 36020, (2016).

[66]   R. Tomasello, M. Ricci, P. Burrascano, V. Puliafito, M. Carpentieri, and G. Finocchio, ''Electrical detection of single magnetic skyrmion at room temperature,'' AIP Adv., **7**, 56022, (2017).

[67]   S. Parkin, and S.-H. Yang, ''Memory on the racetrack,'' *Nat. Nanotechnol.*, 10, 195–198, (2015).

[68]   Y. Zhou, E. Iacocca, A.A. Awad, R.K. Dumas, F.C. Zhang, H.B. Braun, and J. Åkerman, ''Dynamically stabilized magnetic skyrmion,'' *Nat. Commun.*, **6**, 8193, (2015).

[69]   M. Carpentieri, R. Tomasello, R. Zivieri, and G. Finocchio, ''Topological, non-topological and instanton droplets driven by spin-transfer torque in materials with perpendicular magnetic anisotropy and Dzyaloshinskii-Moriya Interaction,'' *Sci. Rep.*, **5**, 16184, (2015).

[70]   G. Finocchio, M. Ricci, R. Tomasello, A. Giordano, M. Lanuzza, V. Puliafito, P. Burrascano, B. Azzerboni, and M. Carpentieri, ''Skyrmion based microwave detectors and harvesting.'' *Appl. Phys. Lett*., **107**, 262401, (2015).

[71]   X. Zhang, ''Magnetic skyrmion logic gates: conversion, duplication and merging of skyrmions,'' *Sci. Rep*., **5**, 9400, (2015).

[72]   D. Pinna, ''Skyrmion Gas Manipulation for Probabilistic Computing,'' 1–41, (2017).

[73]   R. Tomasello, V. Puliafito, E. Martinez, A. Manchon, M. Ricci, M. Carpentieri, and G. Finocchio, ''Performance of synthetic antiferromagnetic racetrack memory: domain wall vs skyrmion,'' *Submitt. to Phys. Rev.*, Appl (2017).

[74]   K.-S. Ryu, S.-H. Yang, L.Thomas, and S. Parkin, ''Chiral spin torque arising from proximity-induced magnetization,'' *Nat. Commun.* **5**, 3910, (2014).

[75]   S.-H. Yang, ''Domain-wall velocities of up to 750 m s-1 driven by exchange-coupling torque in synthetic antiferromagnets,'' *Nat. Nanotechnol*., **10**, 221–226, (2015).

[76]   E. Cardelli, E. Della Torre, and A. Faba, "A general vector hysteresis operator: Extension to the 3-D case," *IEEE Trans. Magn*., **46**, 5560771, (2010).

[77]   E. Cardelli, "A general hysteresis operator for the modeling of vector fields," *IEEE Trans. Magn.*, **47**, 5729829, (2011).

[78]   S. Quondam Antonio, A. Faba, G. Carlotti, and E. Cardelli, "Vector hysteresis model identification for iron-silicon thin films from micromagnetic simulations," *Phys. B: Cond. Matt.*, **486**, 97-100, (2016).

[79]   E. Cardelli, A. Faba, M. Pompei, and S. Quondam Antonio, "Pattern search approach to ferromagnetic material modelling," *Intern. J. Num. Model.: Electr. Net., Dev. and Fields*. (2017).

[80]   G. Siracusano, R. Tomasello, A. Giordano, V. Puliafito, B. Azzerboni, O. Ozatay, M.Carpentieri, G. Finocchio, ''Magnetic Radial Vortex Stabilization and Efficient Manipulation Driven by the Dzyaloshinskii-Moriya Interaction and Spin-Transfer Torque,'' *Phys. Rev. Lett.,* **117**, 87204, (2016).

[81]   G. Siracusano, R. Tomasello, V. Puliafito, A. Giordano, B. Azzerboni, A. La Corte, M. Carpentieri, and G.Finocchio, ''Intrinsic synchronization of an array of spin-torque oscillators driven by the spin-Hall effect,'' *J. Appl. Phys.,* **117**, 17E504, (2015).

[82]   V. Puliafito, A. Giordano, A. Laudani, F. Garescì, M. Carpentieri, B. Azzerboni, and G. Finocchio, "Scalable synchronization of spin-Hall oscillators in out-of-plane field," *Appl. Phys. Lett.*, **109**, 202402, (2016).

[83]   S.-H. Yang, ''Domain-wall velocities of up to 750 m s−1 driven by exchange-coupling torque in synthetic antiferromagnets,'' *Nat. Nanotechnol.*, **10**, 221–226, (2015).

[84]   S. Rohart, and A. Thiaville, ''Skyrmion confinement in ultrathin film nanostructures in the presence of Dzyaloshinskii-Moriya interaction,'' *Phys. Rev. B.*, **88**, 184422, (2013).

[85]   W. F. Brown, ''Thermal Fluctuations of a Single-Domain Particle,'' *Phys. Rev.*, **130**, 1677–1686, (1963)

[86]   R. Tomasello, K. Y. Guslienko, M. Ricci, A. Giordano, J. Barker, M. Carpentieri, O. Chubykalo-Fesenko, and G. Finocchio, "Origin of temperature and field dependence of magnetic skyrmion size in ultrathin nanodots" *Phys. Rev. B*, **97**, 060402 (2018).

[87]   C. Schütte, J. Iwasaki, A. Rosch, and N. Nagaosa, "Inertia, diffusion, and dynamics of a driven skyrmion" *Phys. Rev. B,* **90**, 174434 (2014).

[88]   J. Sinova, S. O. Valenzuela, J. Wunderlich, C. H. Back, and T. Jungwirth, "Spin Hall effects", *Rev. Mod. Phys.* **87**, 1213 (2015).

[89]   W. Jiang, X. Zhang, G. Yu, W. Zhang, X. Wang, M. Benjamin Jungfleisch, J. E. Pearson, X. Cheng, O. Heinonen, K. L. Wang, Y. Zhou, A. Hoffmann, and S. G. E. te Velthuis, "Skyrmion dynamics in width-varying nanotracks and implications for skyrmionic applications", *Nat. Phys. 13, 162 (2016).*

[90]   K. Litzius, I. Lemesh, B. Krüger, P. Bassirian, L. Caretta, K. Richter, F. Büttner, K. Sato, O. A. Tretiakov, J. Förster, R. M. Reeve, M. Weigand, I. Bykova, H. Stoll, G. Schütz, G. S. D. Beach, and M. Kläui, "Skyrmion Hall Effect Revealed by Direct Time-Resolved X-Ray Microscopy", *Nat. Phys.* **13**, 170 (2016).

[91]   G. Yu, P. Upadhyaya, X. Li, W. Li, S. K. Kim, Y. Fan, K. L. Wong, Y. Tserkovnyak, P. K. Amiri, and K. L. Wang, "Room-Temperature Creation and Spin–Orbit Torque Manipulation of Skyrmions in Thin Films with Engineered Asymmetry",*Nano Lett.* **16**, 1981 (2016).

[92]   S. Woo, K. M. Song, X. Zhang, Y. Zhou, M. Ezawa, X. Liu, S. Finizio, J. Raabe, N. J. Lee, S.-I. Kim, S.-Y. Park, Y. Kim, J.-Y. Kim, D. Lee, O. Lee, J. W. Choi, B.-C. Min, H. C. Koo, and J. Chang, "Current-driven dynamics and inhibition of the skyrmion Hall effect of ferrimagnetic skyrmions in GdFeCo films", *Nat. Commun.* **9**, 959 (2018)

[93]   X. Zhang, Y. Zhou, and M. Ezawa, " Magnetic bilayer-skyrmions without skyrmion Hall effect", *Nat. Commun.,***7**, 10293 (2016).

[94]   R. Tomasello, V. Puliafito, E. Martinez, A. Manchon, M. Ricci,M. Carpentieri, and G. Finocchio, " Performance of synthetic antiferromagnetic racetrack memory: domain wall versus skyrmion", *J. Phys. D,* **50**, 325302 (2017).

[95]   J. Barker and O. A. Tretiakov," Static and Dynamical Properties of Antiferromagnetic Skyrmions in the Presence of Applied Current and Temperature", *Phys. Rev. Lett*. **116**, 147203 (2016).

[96]   M. H. Nguyen, D. C. Ralph, and R. A. Buhrman," Spin Torque Study of the Spin Hall Conductivity and Spin Diffusion Length in Platinum Thin Films with Varying Resistivity", *Phys. Rev.Lett*.**116**, 126601 (2016).

[97]   L. Lopez-Diaz, D. Aurelio, L. Torres, E. Martinez, M. A. Hernandez-Lopez, J. Gomez, O. Alejos, M. Carpentieri, G. Finocchio, and G. Consolo, "Micromagnetic simulations using Graphics Processing Units", *J. Phys. D: Appl. Phys*. **45**, 323001 (2012).

[98]   A. Giordano, G. Finocchio, L. Torres, M. Carpentieri, and B.Azzerboni," Skyrmion based microwave detectors and harvesting ", *J. Appl. Phys*.**111**, 07D112 (2012).

[99]   G. Finocchio, I. N. Krivorotov, X. Cheng, L. Torres, and B.Azzerboni, "Micromagnetic understanding of stochastic resonance driven by spin-transfer-torque", *Phys.Rev.B, 83*, 134402 (2011)

[100]   J.-V. Kim and M.-W. Yoo, "Current-driven skyrmion dynamics in disordered films", *Appl. Phys. Lett.* **110**, 132404 (2017).

[101]   W. Wang, M. Beg, B. Zhang, W. Kuch, and H. Fangohr," Driving magnetic skyrmions with microwave fields", *Phys. Rev. B,* **92**, 020403 (2015).

[102]   S.-Z. Lin and A. Saxena, "Noncircular skyrmion and its anisotropic response in thin films of chiral magnets under a tilted magnetic field", *Phys. Rev. B* **92**, 180401 (2015).

[103]   R. Tomasello, A. Giordano, S. Chiappini, R. Zivieri, G. Siracusano, V. Puliafito, I. Medlej, A. La Corte, B. Azzerboni, M. Carpentieri, Z. Zeng, and G. Finocchio," Micromagnetic understanding of the skyrmion Hall angle current dependence in perpendicularly magnetized ferromagnets", *Physical review B*, **98**, 224418 (2018).

[104]   H. Y. Yuan, X. S. Wang, M. Yung, and X. R. Wang, "Wiggling skyrmion propagation under parametric pumping" *arXiv:*1804.07202 (2018)

[105]   See Supplemental Material at http://link.aps.org/supplemental/ 10.1103/PhysRevB.98.224418 for the details of HHT and wavelet transforms, for the micromagnetic framework to calculate the FMR response of the skyrmion, as well as for the four movies.

[106]   E. Gomonay, and V. Loktev, "Spintronics of antiferromagnetic systems (Review Article)", *Low Temperature Physics,* **40**, 17-35, (2014).

[107]   T. Jungwirth, X. Marti, P. Wadley, and J. Wunderlich, "Antiferromagnetic spintronics", *Nature nanotechnology,* **11**, 231-241, (2016).

[108]   V. Baltz, A. Manchon, M. Tsoi, T. Moriyama, T. Ono, and Y. Tserkovnyak, "Antiferromagnetism: the next flagship magnetic order for spintronics?," *arXiv preprint arXiv:1606.04284,* (2016).

[109]   I.Fina, X. Marti, "Electric control of antiferromagnets"*, arXiv :1610.05615v1* [cond mat.mtrl-sci], (2016).

[110]   I J. H. Van Vleck, "Concerning the Theory of Ferromagnetic Resonance Absorption", *Phys. Rev*. **78**, 266 (1950).

[111]   Trounson, Bleil, and Maxwell, **"**Magnetic Resonance in Antiferromagnetic Materials near the Curie Temperature", *Phys. Rev.* **79**, 226 (1950);L. R. Maxwell, talk at Pittsburgh meeting APS, March (1951).

[112]   Charles Kittel, "Introduzione alla Fisica dello Stato Solido ", chapt. 13, pag.384.

[113]   P. H. Siegel, "Terahertz technology", *IEEE Trans. Microwave Theory Tech.* **50**, 910 (2002).

[114]   B. Ferguson and X.-C. Zhang, "Materials for terahertz science and technology", *Nature Mater.* **1**, 26 (2002).

[115]   T.J. Yen, W.J. Padilla, N. Fang, D.C. Vier, D.R. Smith, J.B. Pendry, D.N. Basov, and X. Zhang, "Terahertz magnetic response from artificial materials", *Science* **303**, 1494 (2004).

[116]   J.F. Federici, B. Schulkin, F. Huang, D. Gary, R. Barat, F. Oliveira, and D. Zimdars, Semicond. "THz imaging and sensing for security applications-explosives, weapons and drugs", *Science and Techn.* **20**, S266 (2005).

[117]   C.D. Stoik, M.J. Bohn, and J.L. Blackshire, "Nondestructive evaluation of aircraft composites using transmissive terahertz time domain spectroscopy", *Optics Expr.* **16**, 17039 (2008).

[118]   M. Tonouchi, "Cutting-edge terahertz technology", *Nature Photon.* **1**, 97 (2007).

[119]   W. Withayachumnankul, G.M. Png, and X. Yin, "T-ray sensing and imaging", *Proc. IEEE* **95**, 1528 (2007).

[120]   P.E. Roy, R.M. Otxoa, and J. Wunderlich, "Robust picosecond writing of a layered antiferromagnet by staggered spin-orbit fields", *Phys. Rev. B* **94**, 014439 (2016).

[121]   K. Olejnik, V. Schuler, X. Marti, V. Novák, Z. Kaspar, P. Wadley, R.P. Campion, K.W. Edmonds, B.L. Gallagher, J. Garces, M. Baumgartner, P. Gambardella, and T.

Jungwirth, "Antiferromagnetic CuMnAs multi-level memory cell with microelectronic compatibility", *Nature Comm.* **8**, 15434 (2017).

[122]   A. S. Núñez, R. A. Duine, P. Haney, and A. H. MacDonald, "Theory of spin torques and giant magnetoresistance in antiferromagnetic metals", *Phys. Rev.* B **73**, 214426 (2006).

[123]   T. Moriyama, N. Matsuzaki, K.-J. Kim, I. Suzuki, T. Taniyama, and T. Ono, "Transmission of spin waves in ordered FeRh epitaxial thin films", *Appl. Phys. Lett.* **107**, 122403 (2015).

[124]   L. Liu, T. Moriyama, D. C. Ralph, and R. A. Buhrman, "Spin-torque ferromagnetic resonance induced by the spin Hall effect", *Phys. Rev. Lett.* **106**, 036601 (2011).

[125]   V. Glazkov, T. Soldatov and Yu. Krasnikova, "Numeric calculation of antiferromagnetic resonance frequencies for the noncollinear antiferromagnet", *Appl. Magn. Reson* **47**, 1080 (2016).

[126]   A. Manchon, I.M. Miron, T. Jungwirth, J. Sinova, J. Zelezny, A. Thiaville, K. Garello, and P. Gambardella, "Current-induced spin-orbit torques in ferromagnetic and antiferromagnetic systems", *arXiv:1801.09636* (2018).

[127]   N. Ntallis and K.G. Efthimiadis, "Micromagnetic simulation of an antiferromagnetic particle", *Comp. Mat. Science* **97**, 42 (2015).

[128]   E. V. Gomonay and V. M. Loktev, "Spintronics of antiferromagnetic systems", *Low Temp. Phys.* **40**, 17 (2014).

[129]   S. Baierl, J.H. Mentink, M. Hohenleutner, L. Braun, T.-M. Do, C. Lange, A. Sell, M. Fiebig, G. Woltersdorf, T. Kampfrath, and R. Huber, "Terahertz-driven nonlinear spin response of antiferromagnetic nickel oxide", *Phys. Rev. Lett.* **117**, 197201 (2016).

[130]   R. Khymyn, I. Lisenkov, V. Tiberkevich, B. A. Ivanov, and A. Slavin, "Antiferromagnetic THz-frequency Josephson-like oscillator driven by spin current", *Sci. Rep.* **7**, 43705 (2017).

[131]   V. Puliafito1, R. Khymyn, M. Carpentieri, B. Azzerboni1, V. Tiberkevich, A. Slavin, G. Finocchio, "Micromagnetic modeling of terahertz oscillations in an antiferromagnetic material driven by the spin Hall effect", *Phys.Rev. B.* **99**, 024405 (2019).

[132]   D. Yan, P.X. Yan, G.H.Yue, J.Z.Liu, J.B.Chang, Q.Yang, D.M.Qu, Z.R. Geng, J.T.Chen, G.A.Zhang, and R.F.Zhuo, "Self-assembled flower-like hierarchical spheres and nanobelts of manganese oxide by hydrothermal method and morphology control of them" , *Chem. Phys. Lett.* **440**, 134-138 (2007).

[133]   E. Grootendorst, V. Verbeek, and V. Ponec, "The Role of the Mars and Van Krevelen Mechanism in the Selective Oxidation of Nitrosobenzene and the Deoxygenation of Nitrobenzene on Oxidic Catalysts", *J catal.* **157**, 706 (1995).

[134]   W. Weimin, Y. Yongnian, and Z.Jiayu, "Selective reduction of nitrobenzene to nitrosobenzene over different kinds of trimanganese tetroxide catalysts*", App. Catal.A.* **133**, 81, (1995).

[135]   Chugai electric industrial Co. Ltd., *Japan Pat. Appl.* **82**, 209-883 (1982).

[136]   A. Robert Armstrong, and Peter G. Bruce "Synthesis of layered LiMnO2 as an electrode for rechargeable lithium batteries", *Nature,* **381**, 499–500 (1996).

[137]   B. Tarascon, J-M. Angew, "Nanomaterials for rechargeable lithium batteries", *Chem. Int. Ed.*, **47**, 2930-2946 (2008).

[138]   T.E. Moore, M. Ellis, P.W. Selwood, "Solid Oxides and Hydroxides of Manganese", *Journal of the American Chemical Society*, **856** (1950).

[139]   I.V. Solovyev, K. Terakura, ""Effective single-particle potentials for MnO in light of interatomic magnetic interactions: Existing theories and perspectives", *Phys. Rev. B.* **58**, 15496 (1998).

[140]   S.K. Nayak, P.J. Jena, "Equilibrium geometry, stability, and magnetic properties of small MnO clusters", *J. Am. Chem. Soc.* 121, 644 (1999).

[141]   S. G. Sanfélix "Manganese Oxide Nanoparticles: Synthesis and Magnetic Properties", report (2008).

[142]   Book of Subvolume D 'Non-Tetrahedrally Bonded Binary Compounds II' of Volume 41 'Semiconductors' of Landolt-Börnstein - Group III Condensed Matter.

[143]   J. Rodríguez Carvajal, "Recent advances in magnetic structure determination by neutron powder diffraction + FullProf ", *Phys. B* **192** 55 (1992).

[144]   M. Ghosh, K. Biswas, A. Sundaresan, and C.N.R. Rao "MnO and NiO nanoparticles: Synthesis and magnetic proprties", *J.M.Chem*. 16, 106-111 (2006)